AN ABSTRACT OF THE THESIS OF

Jordan Michael Bauman for the degree of Master of Science in Physics presented on August 14, 2002.

Title: Classical Chaotic Scattering from Symmetric Four Hill Potentials

Abstract approved: Redacted for Privacy

Rubin H. Landau

Classical chaotic scattering experiments were performed on ten different four hill potentials, unique under x-axis reflection, given by:

$V(x,y) = x^2y^2e^{-(x^2+y^2)}\sigma_i$ where σ_i was ± 1 depending upon quadrant. Our work was based on a paper (9) that only studied the case where $\sigma_i = 1$ in all quadrants. The system used was a time independent Hamiltonian with energy conservation.

Chaos manifested itself in our experiment in two ways. First, below some critical energy, particles would become almost trapped by the system. Second, above the critical energy, the particles directly strike the saddle point.

Trajectories were integrated using a standard 4^{th} order Runge-Kutta ODE solver. Scattering angle and time delay were measured as a function of the impact parameter. Chaos was seen in these scattering functions as discontinuities. The Lyapunov exponent was measured for a number of energies using a brute force method (separation of nearby trajectories). The capacity dimension was measured using the uncertainty exponent method (13).

The critical energy was measured using both capacity dimension and Lyapunov exponent data. Five of the potentials had a critical energy within error bounds of E_c=0.039: V_{2C}, V_3, V_{4A}, V_{4B}, V_6. Three were with error bounds of E_c=0.135: V_1, V_{2A}, V_{5B}. Potential V_{2B} had a value of 0.071 and V_{5A} had 0.092.

All bifurcations in this system were abrupt. Three of the potentials were generic abrupt: V_1, V_{2A}, V_{5B}. Six of the potentials had abrupt crisis bifurcations: V_{2B}, V_{2C}, V_3, V_{4A}, V_{4B}, V_6. Potential V_{5A} had abrupt nonhyperbolic bifurcations.

The Lyapunov exponent for all ten potentials had a linear high energy behavior that had not been seen before. The systems showed chaos and the largest Lyapunov exponents for them were measured (below the critical energy) to be: V_1=0.446 ± 0.013, V_{2A}=0.472 ± 0.007, V_{2B}=0.663 ± 0.007, V_{2C}=0.683 ± 0.010, V_3=0.655 ± 0.011, V_{4A}=0.714 ± 0.010, V_{4B}=0.743 ± 0.003, V_{5A}=0.741 ± 0.009, V_{5B}=0.461 ± 0.006, V_6=0.697 ± 0.008.

We then concluded that systems that contained attractors were more chaotic than the one that did not. In addition, we saw that the sign of the hills on the left side of the system governed the shape of the scattering functions but not all of the chaotic characteristics.

Classical Chaotic Scatting from Symmetric Four Hill Potentials

by
Jordan Michael Bauman

A THESIS

submitted to

Oregon State University

in partial fulfillment of
the requirements for the
degree of

Master of Science

Presented August 14, 2002
Commencement June 2003

Master of Science thesis of Jordan Michael Bauman presented on August 14, 2002.

APPROVED

Redacted for Privacy

Major Professor, representing Physics

Redacted for Privacy

Head of the Department of Physics

Redacted for Privacy

Dean of Graduate School

I understand that my thesis will become part of the permanent collection of Oregon State University Libraries. My signature below authorizes release of my thesis to any reader upon request.

Redacted for Privacy

Jordan Michael Bauman, Author

ACKNOWLEDGEMENTS

The road has been a very long and hard one. Many times, I was positive that I was not going to make it. In the time it took to complete this work, there have been health problems, two untreatable diseases, two near death experiences, family illnesses, three major professors, computer crashes, clerical errors, financial hardships, and a host of other problems.

Throughout this thesis will be a single word: "we". Even though I designed the project, coded it, and wrote this thesis, the word is appropriate. Without a lot of people, this simply would not have been completed. If I have forgotten anyone, it is due to failing memory rather than intentional oversight.

For reasons that I will never know (or understand) Dr. Rubin Landau took a problem student like myself under his wing. His strange blend of support, encouragement, and a sharp motivational stick has been appreciated more than I can express. I thank him for his calmness in the face of panicked 5 a.m. emails, frantic telephone calls, and endless web page updates. He has taught me to truly understand the phrase "that's research".

Sometimes in life people give you a second chance. It is seldom to find a person willing to give you three of them. I was lucky that Dr. Al Stetz is such a person. It is because of him that I was accepted into the Physics department and survived my first year. I will never forget having coffee with him (well before my eyes were usually open) so he could make sure that I really wanted to be a physicist. He has taught me that there is more to life than work, but you would be a fool to hate what you do for a living.

Dr. Henri Jansen has been very supportive of me as well. Without him I would never have ended up in computational physics in the first place. It was too bad we never figured out why GIAMES could not correctly calculate a simple potential well. He taught me that a computer could turn out gigs of garbage in a heartbeat, so you had better know what it is doing. He also taught me to never be a slave to your tools. Use what works the best whenever you can; even if it is just a spreadsheet.

There are numerous instructors that I have had that have shaped the way I think. Each has contributed a small piece of their enormous knowledge in the hopes of making a decent scientist out of me. These are scientists of a caliber I hope to be some day: Drs. Tate, Manogue, McIntyre, Seimens, Wasserman, Giebultowicz, and Hetherington. A special thanks goes to Dr. Adel Faridani. It is from him that I learned almost everything I know about numerical methods. While he made me work very hard to understand the theory of what I do, I am better off for it. I will always be a better scientist than student, but I appreciate the effort that these people have put in for me.

Without my family and friends I would not have been able to make it through the hard times, or enjoyed the good times. I give my thanks to those who have supported me when I'm putting in the long hours and the sleepless nights. Dorinda Morton for her support and kindness, my brother Paul for giving me something else to think about than work, John Griffith for getting me into this field in the first place, Ivar and Bjørg Berge for an incredible amount of financial and emotional support, and my parents for their love (even when they don't understand what I do).

Finally, I simply could not have come this far without my wife, Anja. She's been everything that I could have asked for and many things I should have. Her support, love, and belief that I could complete my thesis, made the difference. For that I thank her.

TABLE OF CONTENTS

TABLE OF CONTENTS (Continued)

TABLE OF CONTENTS (Continued)

LIST OF FIGURES

LIST OF FIGURES (continued)

LIST OF FIGURES (continued)

LIST OF TABLES

DEDICATION

For Bellana Thyra Berge Bauman, who has taught me that simple pleasures are often the best kind.

Classical Chaotic Scatting from Symmetric Four Hill Potentials

1. INTRODUCTION

In this section we give a short introduction to chaos theory and chaotic scattering in general. We also present a brief overview of a previous experiment and introduce our experiment. In Section 2, we give the specific potentials and equations used in our scattering experiments. Section 3 covers our measurement of chaotic behavior. The details of our methods are given in Section 4. Finally, results and conclusions are presented in Sections 5 and 6.

1.1. BASICS OF CHAOS

Chaos can be thought of as an extreme sensitivity to initial conditions. A small change in the initial state of the system results in extremely large changes in the final state. In highly chaotic systems, it is easy to mistake this for random behavior called noise. Chaos can be found in a number of different places.

> Chaotic behavior seems to be universal - it shows up in mechanical oscillators, electrical circuits, lasers, nonlinear optical system, chemical reactions, nerve cells, heated fluids, and many other systems (1).

Systems that produce chaos are not required to have complex equations, however, they must be non-linear. In a linear system, a small change in input would give a small change in output.

Chaotic systems often have a point of bifurcation. A bifurcation is a set of initial conditions that divide the behavior into two parts. Above the bifurcation the systems acts one way and below it acts another. A system can have more than one bifurcation. A bifurcation is often accompanied by a change in system response.

While these systems may seem noisy (random), chaos can be seen in completely deterministic systems that have no noise (besides numerical precision). Deterministic means that knowledge of the equations of motion, initial conditions, and system parameters entirely define the system. By studying the system's geometric (Section 3.2) and transient properties (Section 3.3), it is possible to distinguish a chaotic system from a noisy one.

1.2. CLASSICAL CHAOTIC SCATTERING

We can roughly define scattering as the problem of obtaining the relationship between an input variable and an output variable in a dynamical, usually Hamiltonian, system. The input variable represents the initial state of the system and the output variable represents its "final" state. For our system we used a point particle in a two dimensional potential. The potential is very small outside a well defined scattering region, where the particle moves in approximately straight lines (2).

In a scattering experiment, the particle is incident from infinity, interacts with the system, and eventually exits the scattering region (to infinity). A stylized scattering experiment is shown in Figure 1.

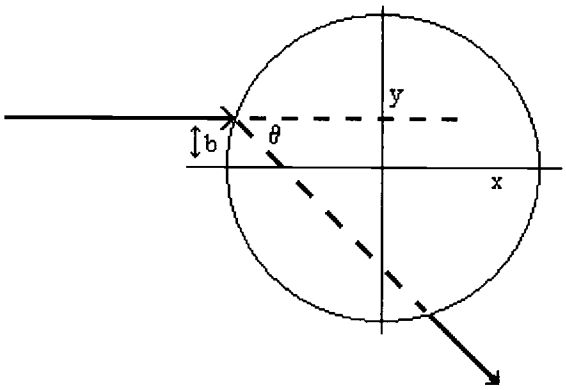

Figure 1.1 – A basic scattering experiment.

Note that we have drawn the particle coming in parallel to the x-axis. While this is not necessary, it is the most common setup used for classical chaotic scattering. The quantity, b, is called the impact parameter, the circle represents the scattering region, and θ is called the scattering angle. This is the angle between the undeflected input path and the exit path. The length of time it takes for the particle to leave the system is called the delay time, t_d. In a scattering experiment, the output values (either θ or t_d) are plotted as a function of the input variable (usually b).

As mentioned earlier, chaos can be thought of as an extreme sensitivity to initial conditions. In scattering experiments, we see this when the scattering angle (or delay time) changes rapidly with small changes in impact parameter. This is the hallmark of chaos. As we will show in Section 5.1, when the system is chaotic, the scattering plots will have regions that are discontinuous.

In a bound system, the particle will experience the effects of the potential for an infinite amount of time. Chaos will manifest itself once the system "settles down" and the transients die out. This is in stark contrast to a scattering system where the particle spends a finite amount of time near the potential. It is for this reason that chaos in a scattering system is considered a transient effect.

Chaos arises in one of two ways in a scattering system. The first way is the particle striking the potential center directly. The second, and most interesting, results when the particle becomes almost trapped inside the system (3). In section 3, we will show how to experimentally differentiate between these two routes.

Chaotic scattering is not confined to the realm of theoretical systems, it has been observed in a variety of physical systems. These systems include (but are not limited to): atomic scattering (4), three body gravitational problems (5), chemical reactions (6), electron transport (7), and fluid dynamics (8).

1.3. BLEHER, GREBOGI, AND OTT'S CHAOTIC SCATTERING EXPERIMENT

Much of our work comes from expanding upon the ideas and techniques in a paper by Bleher, Grebogi, and Ott (9). They used the potential:

$$V(x,y) = x^2y^2e^{-(x^2+y^2)} \qquad [1.3\text{-}1]$$

This is a symmetric four hill potential centered at the origin. A mesh plot of this is shown in Figure 1.2.

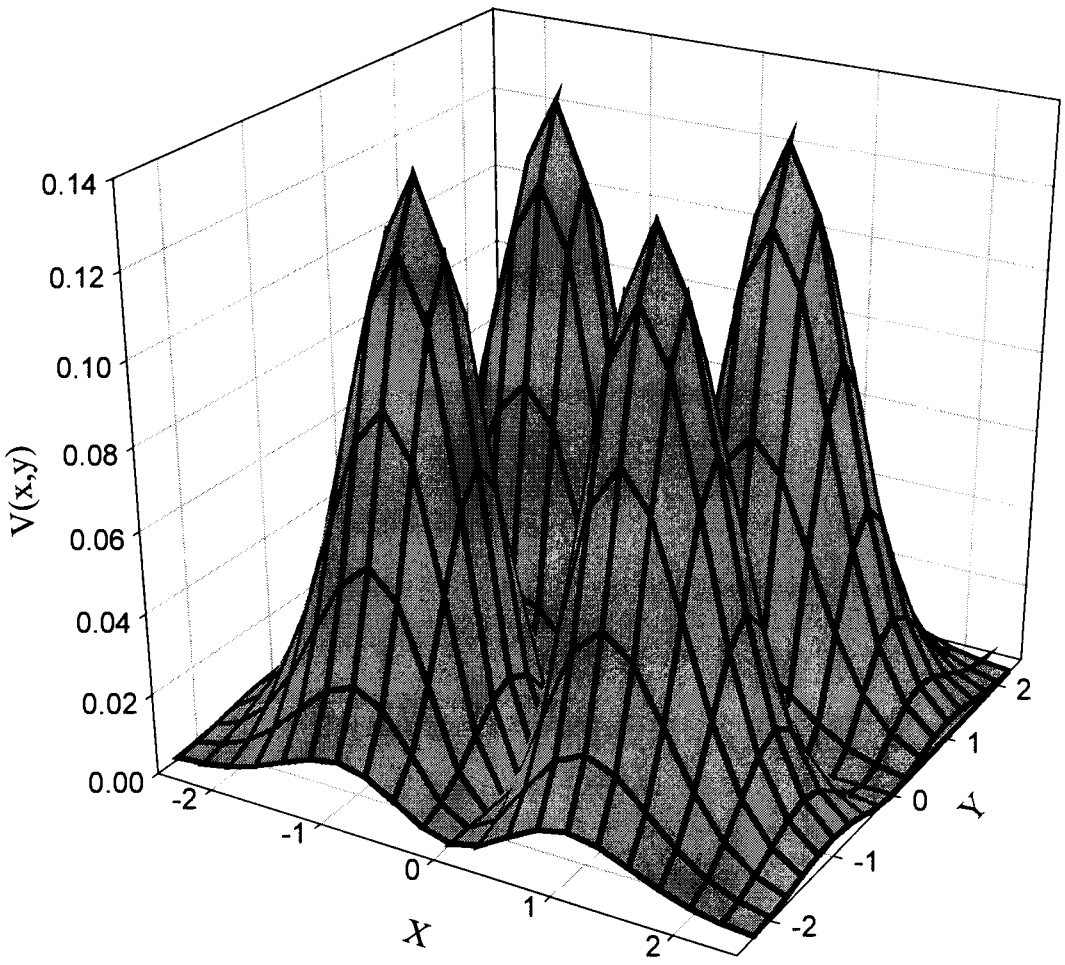

Figure 1.2 – Three-dimensional plot of Equation 1.3-1.

Note that the peak maximums are centered at $x = \pm 1$, $y = \pm 1$ and have a value of e^{-2}, with one peak in each quadrant. This is more apparent from a contour plot shown below:

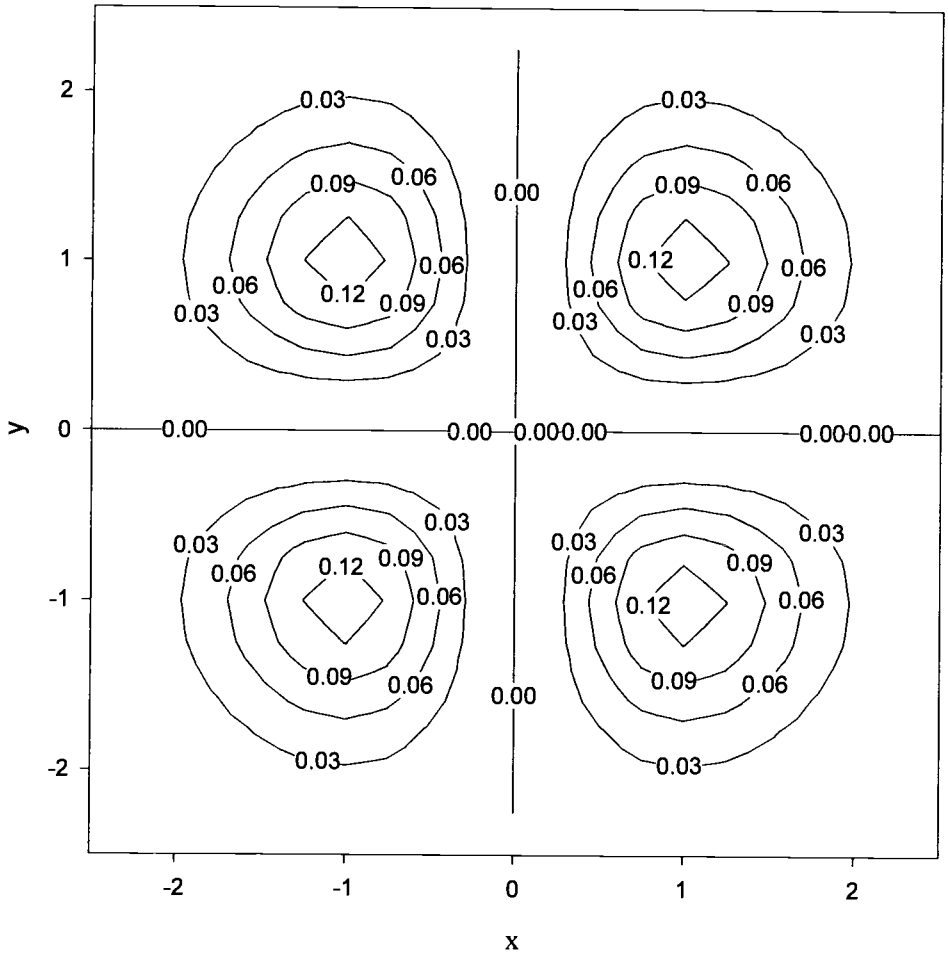

Figure 1.3 - Contour plot of Equation 1.3-1.

The potential of Equation 1.3-1 has been well studied (9,10). The values found previously (9) for the scattering angle, delay time, transient properties, and geometric properties, were verified using our methods (Section 4).

1.4. OUR EXPERIMENT

The main idea for our project did not come from the literature, but from our course work. In the winter of 2001, we took a course in computational physics from Dr. Rubin Landau at Oregon State University. We were assigned a project to study the chaotic behavior from potential scattering. The potential suggested was that of Equation 1.3-1. However, for curiosity's sake, we became interested in looking at a pair of symmetric dipoles. We found a potential that had the exact same magnitude as the original, but had opposite sign in Quadrants III and I.

After we completed this project, it was suggested that we investigate the new potential in detail for our thesis. In the process of finding this symmetric dipole potential, we found a way to make eight more unique potentials that were similar. In Section 2.2, we will go into more detail about these nine potentials that we studied.

During our literature search, it became apparent to us that none of these new potentials had been studied. We wanted to "complete" this amazingly simple (yet complex) potential. So, we set out to characterize these new potentials using geometric and transient properties (Sections 3.2 and 3.3). We were also interested in some of the internal structural details about how chaos originates in these systems (Section 3.1).

Our system is very unique. Using the potentials given in Section 2.2, we could change the sign of an individual peak (Figures 1.2 and 1.3) at will. This allowed us to smoothly transition the system from the pure repulsive potential of Equation 1.3-1 to a purely attractive potential (the negative of Equation 1.3-1). We wanted to take advantage of this and investigate if the system became more chaotic as we added attractive potentials.

2. EQUATIONS OF MOTION

In this section, we focus upon the equations of motion for our system. Since our system is classical, we use Hamilton's equations. We also go into detail of the ten potentials that were studied (Equation 1.3-1 and nine similar ones).

2.1. THE HAMILTONIAN SYSTEM

Hamiltonian systems are also known as conservative systems. Conservative means that there are physical properties of the system that do not change over time. In our experiment we have no energy dissipation, so total energy is conserved and the Hamiltonian is simply the sum of kinetic and potential energy (also called mechanical energy):

$$H = T + U \qquad [2.1\text{-}1]$$

where T is the kinetic energy and U is the potential energy. We rewrite this equation in the standard coordinate notation, substituting the kinetic energy for a point particle:

$$H(\vec{q},\vec{p}) = \frac{|\vec{p}|^2}{2m} + V(\vec{q}) \qquad [2.1\text{-}2]$$

where m is the mass of the particle, $\vec{q}$ represents the position vector, $\vec{p}$ represents the momentum vector, and $V(\vec{q})$ is the potential function (discussed in more detail in Section 2.2).

The solution to Equation 2.1-2 can be found using Hamilton's method. This results in a set of coupled differential equations given by:

$$\frac{dq_i}{dt} = \frac{\partial H(\vec{q},\vec{p})}{\partial p_i} \qquad [2.1\text{-}3a]$$

$$\frac{dp_i}{dt} = -\frac{\partial H(\vec{q},\vec{p})}{\partial q_i} \qquad [2.1\text{-}3b]$$

where q_i is the i^{th} position coordinate and p_i is the i^{th} momentum coordinate. This interconnected relationship between the derivatives is referred to as symplectic.

We are now ready to apply these equations to our specific system. First we write the momentum vector in terms of its x and y components:

$$H(\vec{q},\vec{p}) = \frac{\left| p_x\hat{i} + p_y\hat{j} \right|^2}{2m} + V(x,y) = \frac{p_x^2 + p_y^2 + 2p_x\hat{i}\bullet p_y\hat{j}}{2m} + V(x,y) \Rightarrow$$

$$H(\vec{q},\vec{p}) = \frac{p_x^2 + p_y^2}{2m} + V(x,y) \qquad [2.1\text{-}4]$$

The dot product between $\hat{i}$ and $\hat{j}$ is zero because they are orthogonal.

Using the substitutions that $q_1 = x$, $q_2 = y$, $p_1 = p_x$ and $p_2 = p_y$, we generate the four coupled differential equations:

$$\frac{dx}{dt} = \frac{\partial H(\vec{q},\vec{p})}{\partial p_x} = \frac{p_x}{m} \qquad [2.1\text{-}5a]$$

$$\frac{dy}{dt} = \frac{\partial H(\vec{q},\vec{p})}{\partial p_y} = \frac{p_y}{m} \qquad [2.1\text{-}5b]$$

$$\frac{dp_x}{dt} = -\frac{\partial H(\vec{q},\vec{p})}{\partial x} = -\frac{\partial V}{\partial x} \qquad [2.1\text{-}5c]$$

$$\frac{dp_y}{dt} = -\frac{\partial H(\vec{q},\vec{p})}{\partial y} = -\frac{\partial V}{\partial y} \qquad [2.1\text{-}5d]$$

We can eliminate the momentum terms by using the relation between momentum and velocity (and velocity and the position coordinates):

$$p_i = m\frac{dq_i}{dt} \qquad [2.1\text{-}6]$$

Equations 2.1-5a and 2.1-5b equal unity, but Equations 2.1-5c and 2.1-5d become:

$$m\frac{d^2x}{dt^2} = -\frac{\partial V}{\partial x} \qquad [2.1\text{-}7a]$$

$$m\frac{d^2y}{dt^2} = -\frac{\partial V}{\partial y} \qquad [2.1\text{-}7b]$$

The above could also have been derived using Newton's second law:

$$\sum \vec{F} = m\vec{a} = m(a_x\hat{i} + a_y\hat{j}) = m\left(\hat{i}\frac{d^2x}{dt^2} + \hat{j}\frac{d^2y}{dt^2}\right) \qquad [2.1\text{-}8]$$

and the relation between force and potential:

$$\vec{F} = -\vec{\nabla}V = -\hat{i}\frac{\partial V}{\partial x} - \hat{j}\frac{\partial V}{\partial y} \qquad [2.1\text{-}9]$$

Combining Equations 2.1-8 and 2.1-9 together yield:

$$m\left(\hat{i}\frac{d^2x}{dt^2} + \hat{j}\frac{d^2y}{dt^2}\right) = -\hat{i}\frac{\partial V}{\partial x} - \hat{j}\frac{\partial V}{\partial y} \qquad [2.1\text{-}10]$$

Finally, separation of variables results in Equations 2.1-7a and 2.1-7b.

We now focus on writing equations of motion in terms of x and y (and their respective derivatives). The potentials for our experiment are exactly the same as in Equation 1.3-1, with the exception of a leading constant, σ_i:

$$V(x,y) = x^2 y^2 e^{-(x^2+y^2)} \sigma_i \qquad [2.1\text{-}11]$$

where σ_i (± 1 depending on quadrant) sets the sign of the potential hill in different quadrants. The exact value of σ_i will be discussed in Section 2.2. Since Equations 2.1-7a and 2.1-7b require the partial derivative of the potential, we perform that separately:

$$-\frac{\partial V}{\partial x} = \left(2xy^2 e^{-(x^2+y^2)} - 2x^3 y^2 e^{-(x^2+y^2)} \right) \sigma_i \qquad [2.1\text{-}12a]$$

$$-\frac{\partial V}{\partial y} = \left(2x^2 y\, e^{-(x^2+y^2)} - 2x^2 y^3 e^{-(x^2+y^2)} \right) \sigma_i \qquad [2.1\text{-}12b]$$

We factor out V(x,y) (Equation 2.1-11) from these two equations:

$$-\frac{\partial V}{\partial x} = \left(\frac{1}{x} - x \right) 2x^2 y^2 e^{-(x^2+y^2)} \sigma_i = V(x,y)\, 2\left(\frac{1}{x} - x \right) \qquad [2.1\text{-}13a]$$

$$-\frac{\partial V}{\partial y} = \left(\frac{1}{y} - y \right) 2x^2 y^2 e^{-(x^2+y^2)} \sigma_i = V(x,y)\, 2\left(\frac{1}{y} - y \right) \qquad [2.1\text{-}13b]$$

These equations are more elegant and faster to compute. There is also a reduction in flops (floating point operations) from 56 in calculating Equations 2.2-12a and 2.2-12b to 36 in using the two equations above. They do, however, create a

singularity at x = 0 or y = 0. We use the limit of Equations 2.1-12a and 2.1-12b to calculate the derivatives at x = 0 and y=0.

$$\lim_{x\to 0}\left[-\frac{\partial V}{\partial x}\right]=\left(2(0)y^2e^{-((0)^2+y^2)}-2(0)^3y^2e^{-((0)^2+y^2)}\right)\sigma_i=0 \quad [2.1\text{-}14a]$$

$$\lim_{x\to 0}\left[-\frac{\partial V}{\partial y}\right]=\left(2(0)^2y\,e^{-((0)^2+y^2)}-2(0)^2y^3e^{-((0)^2+y^2)}\right)\sigma_i=0 \quad [2.1\text{-}14b]$$

$$\lim_{y\to 0}\left[-\frac{\partial V}{\partial x}\right]=\left(2x(0)^2e^{-(x^2+(0)^2)}-2x^3(0)^2e^{-(x^2+(0)^2)}\right)\sigma_i=0 \quad [2.1\text{-}14c]$$

$$\lim_{y\to 0}\left[-\frac{\partial V}{\partial y}\right]=\left(2x^2(0)\,e^{-(x^2+(0)^2)}-2x^2(0)^3e^{-(x^2+(0)^2)}\right)\sigma_i=0 \quad [2.1\text{-}14d]$$

which generalize to:

$$\lim_{q_i\to 0}\left[-\frac{\partial V}{\partial q_i}\right]=0 \quad [2.1\text{-}14e]$$

where q_i is the position coordinate. Using Equation 2.1-14e, the singularities of Equations 2.1-13a and 2.1-13b are trivial.

By substituting equations 2.1-13a and 2.1-13b into Equations 2.1-7a and 2.1-7b, we are finally able to write the equations of motion in terms of x and y:

$$\frac{d^2x}{dt^2}=\frac{1}{m}V(x,y)\,2\left(\frac{1}{x}-x\right) \quad [2.1\text{-}15a]$$

$$\frac{d^2y}{dt^2}=\frac{1}{m}V(x,y)\,2\left(\frac{1}{y}-y\right) \quad [2.1\text{-}15b]$$

These two second order differential equations (ODEs) will be reduced into a set of four first order ODEs in Section 4.1.

A special comment should be made about the time evolution of the Hamiltonian (Equation 2.1-2). Even though the coordinate vectors, p and q, have time dependence, it is important to realize that Hamiltonian does not. It is completely described (and thus deterministic) if the time dependence of x, y, p_x, and p_y are known. This can be shown formally (discussion parallels that of Reference 11) using the chain rule of calculus:

$$\frac{dH(\vec{q},\vec{p})}{dt} = \sum_{i=1}^{N} \frac{\partial H}{\partial q_i}\frac{dq_i}{dt} + \sum_{i=1}^{N} \frac{\partial H}{\partial p_i}\frac{dp_i}{dt} + \frac{\partial H}{\partial t} \qquad [2.1\text{-}16]$$

using Equations 2.1-3a and 2.1-3b (definitions of the momentum and position coordinates) this becomes:

$$\frac{dH(\vec{q},\vec{p})}{dt} = \sum_{i=1}^{N} \frac{\partial H}{\partial q_i}\frac{\partial H}{\partial p_i} + \sum_{i=1}^{N} \frac{\partial H}{\partial p_i}\left(-\frac{\partial H}{\partial q_i}\right) + \frac{\partial H}{\partial t} \Rightarrow$$

$$\frac{dH(\vec{q},\vec{p})}{dt} = \sum_{i=1}^{N}\left(\frac{\partial H}{\partial q_i}\frac{\partial H}{\partial p_i} - \frac{\partial H}{\partial q_i}\frac{\partial H}{\partial p_i}\right) + \frac{\partial H}{\partial t} = \frac{\partial H}{\partial t} \qquad [2.1\text{-}17]$$

Since our Hamiltonian does not have explicit time dependence, it remains constant over time and energy is conserved (as we stated in Equation 2.1-1). Because we know the time dependence of q and p, we have a deterministic system.

2.2. EXPERIMENTAL POTENTIALS

We needed potentials comparable to the known all positive potential of Equation 1.3-1. The ideal solution was potentials that had exactly the same magnitude as the all positive case, but different sign in select quadrants. By recognizing that x and y have different signs in different quadrants, we were able to take advantage of this and develop a "switch", σ_i. This is the same σ_i used in Equation 2.1-11 and best understood with an example. First we recall Equation 1.3-1 (which has been renamed V_1):

$$V_1(x,y) = x^2 y^2 e^{-(x^2+y^2)} \qquad [2.2\text{-}1]$$

Suppose we wanted a potential that had the same magnitude as Equation 1.3-1, but that was negative in Quadrants I and IV. The sign of x is positive in Quadrants I and IV, and negative in the two others. Using this information, and matching it to the Equation 2.1-11, we call this V_{2A}:

$$V_{2A}(x,y) = x^2 y^2 e^{-(x^2+y^2)} \text{sign}(-x) \qquad [2.2\text{-}2]$$

where we have set σ_i = sign(-x). We made a surface plot of this potential in Figure 2.1.

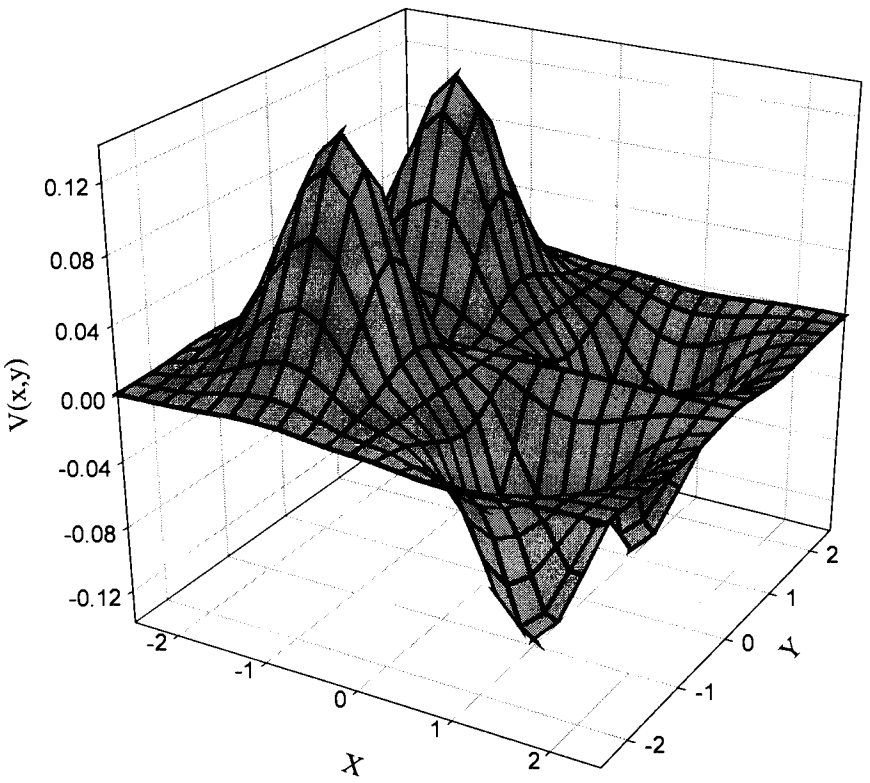

Figure 2.1 – Three-dimensional mesh plot of V_{2A} (Equation 2.2-2).

In order to standardize our routines, all particles are incident from the left. In addition we made sure that, and all potential peaks are centered at (±1,±1). To investigate the other two symmetry possibilities, we had to rotate V_{2A}. These two new potentials were named V_{2B} and V_{2C}; their Equations are given below:

$$V_{2B}(x,y) = x^2y^2e^{-(x^2+y^2)}\text{sign}(x) \qquad [2.2\text{-}3]$$

$$V_{2C}(x,y) = x^2y^2e^{-(x^2+y^2)}\text{sign}(y) \qquad [2.2\text{-}4]$$

These two potentials were then plotted.

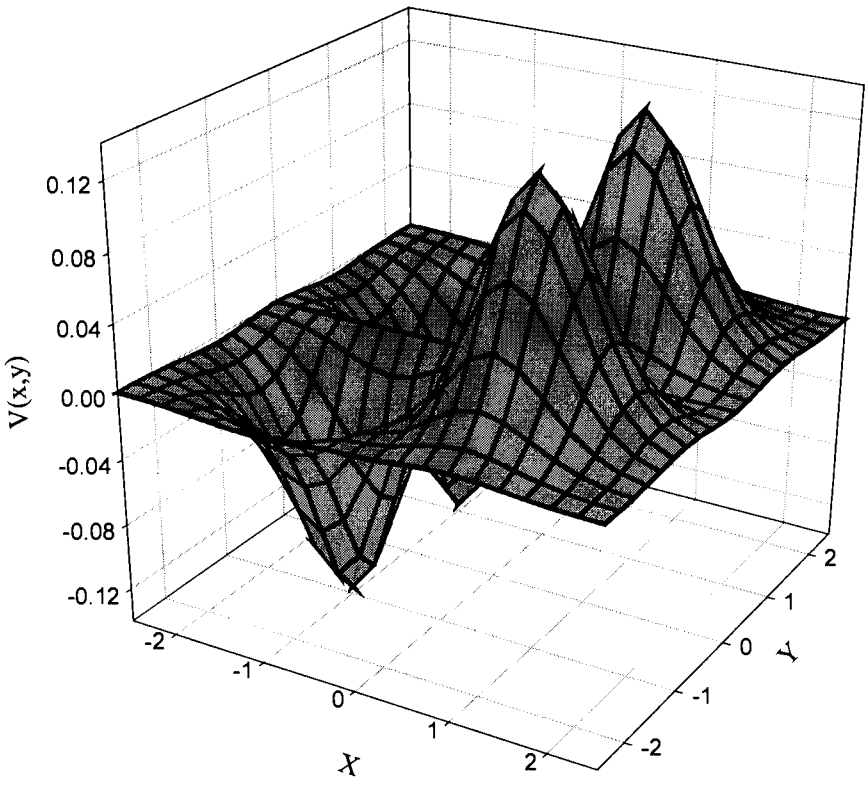

Figure 2.2 – Three-dimensional mesh plot of V_{2B} (Equation 2.2-3).

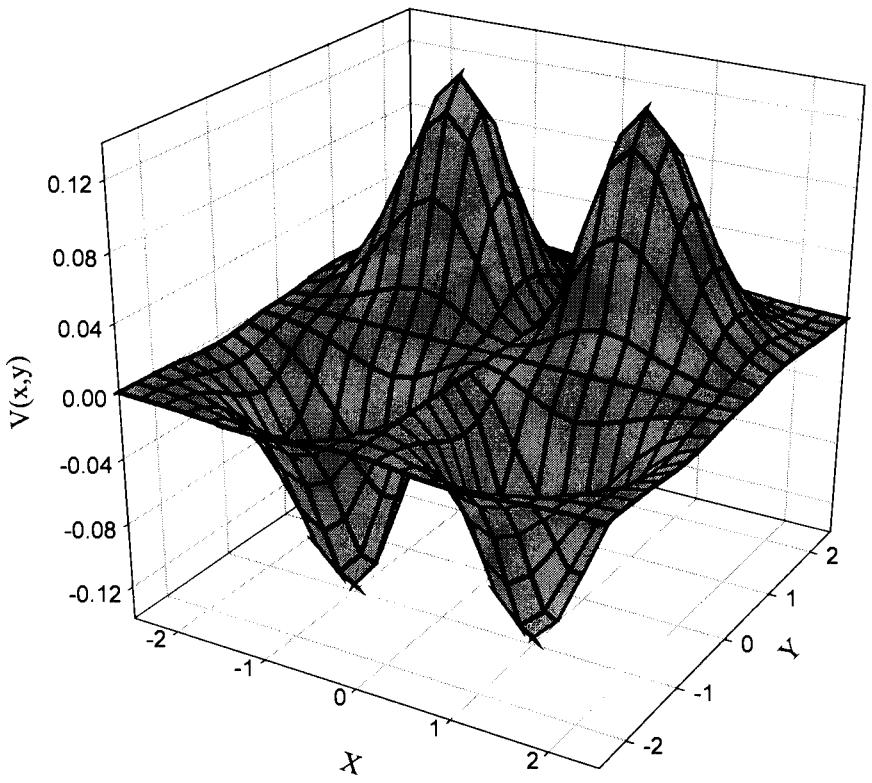

Figure 2.3 – Three-dimensional mesh plot of V_{2C} (Equation 2.2-4).

The last potential that had two positive and two negative hills was the symmetric dipole potential given by Equation 2.2-5. This is the potential that we were referring to in Section 1.4.

$$V_3(x,y) = x^2 y^2 e^{-(x^2+y^2)} \text{sign}(-xy) \qquad [2.2\text{-}5]$$

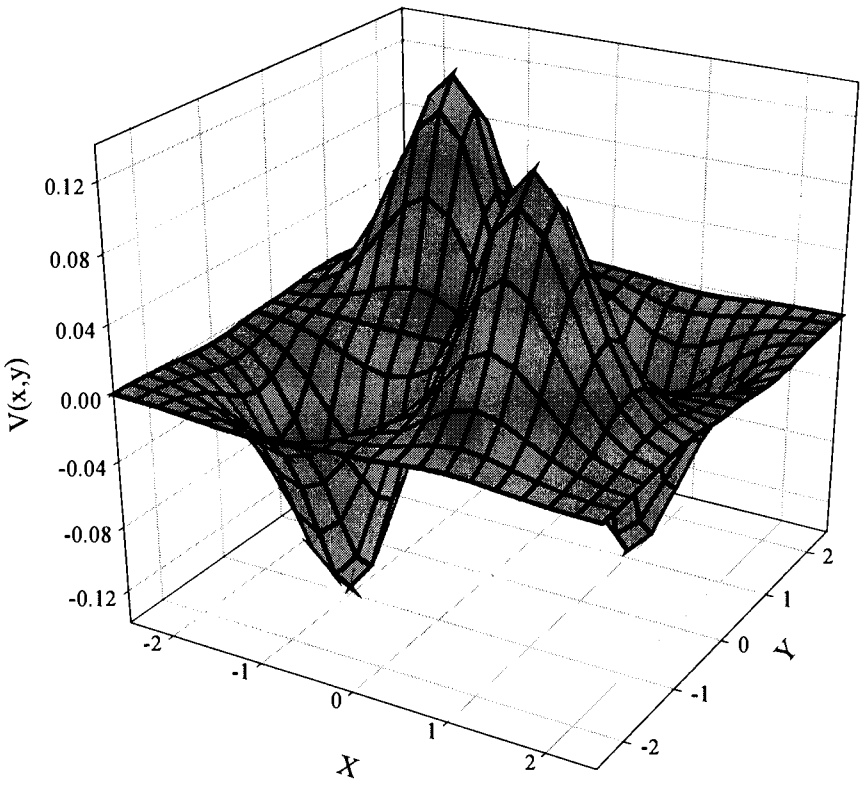

Figure 2.4 – Three-dimensional mesh plot of V_3 (Equation 2.2-5).

We found two potentials, V_{4A} and V_{4B}, which had three negative hills. The σ_i value for these involves multiple sign functions, but works the same as before:

$$V_{4A}(x,y) = x^2 y^2 e^{-(x^2+y^2)}\left[\frac{-1-\text{sign}(x)+\text{sign}(y)-\text{sign}(xy)}{2}\right] \quad [2.2\text{-}6]$$

$$V_{4B}(x,y) = x^2 y^2 e^{-(x^2+y^2)}\left[\frac{-1+\text{sign}(x)+\text{sign}(y)+\text{sign}(xy)}{2}\right] \quad [2.2\text{-}7]$$

These two potentials were plotted the same way as previously.

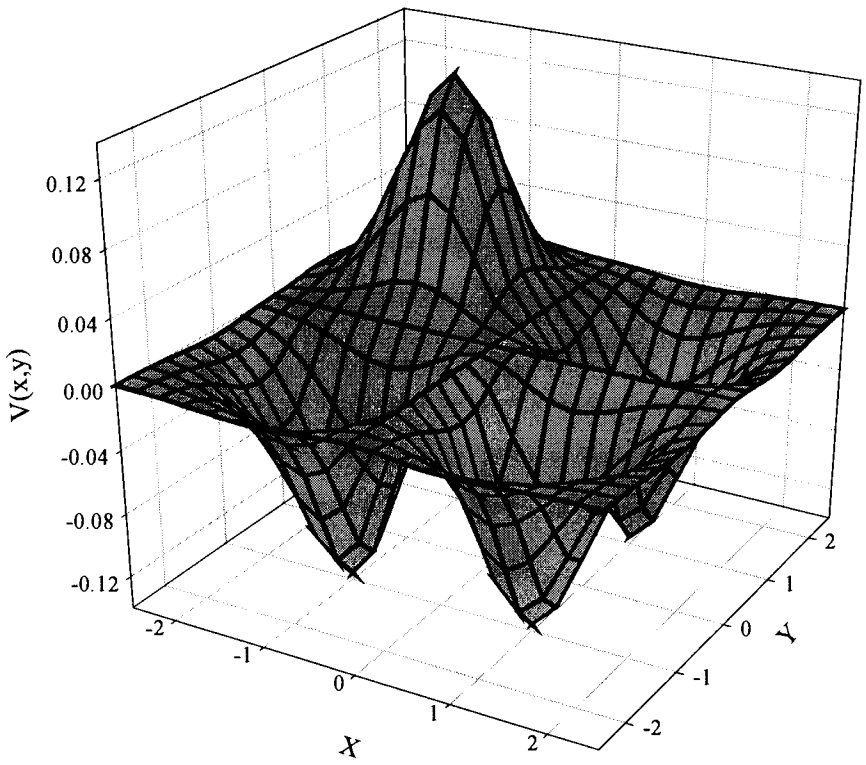

Figure 2.5 – Three-dimensional mesh plot of V_{4A} (Equation 2.2-6).

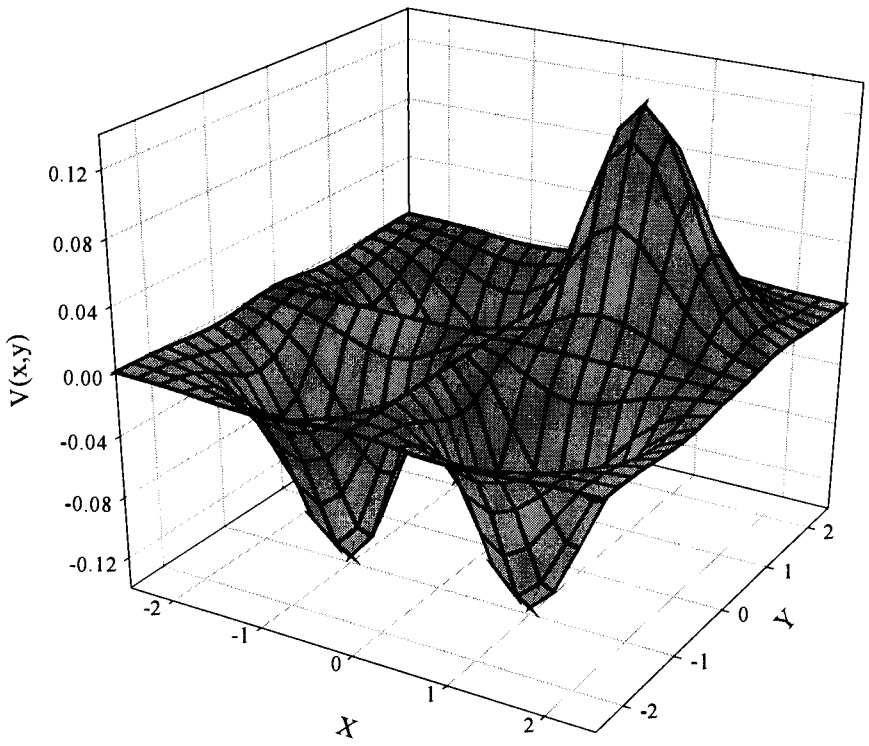

Figure 2.6 – Three-dimensional mesh plot of V_{4B} (Equation 2.2-7).

Next, we present the potentials that have three positive hills, V_{5A} and V_{5B}:

$$V_{5A}(x,y) = x^2 y^2 e^{-(x^2+y^2)}\left[-\frac{-1-\text{sign}(x)-\text{sign}(y)+\text{sign}(xy)}{2}\right] \quad [2.2\text{-}8]$$

$$V_{5B}(x,y) = x^2 y^2 e^{-(x^2+y^2)}\left[-\frac{-1+\text{sign}(x)+\text{sign}(y)+\text{sign}(xy)}{2}\right] \quad [2.2\text{-}9]$$

Three-dimensional plots for these two equations are shown in Figures 2.7 and 2.8:

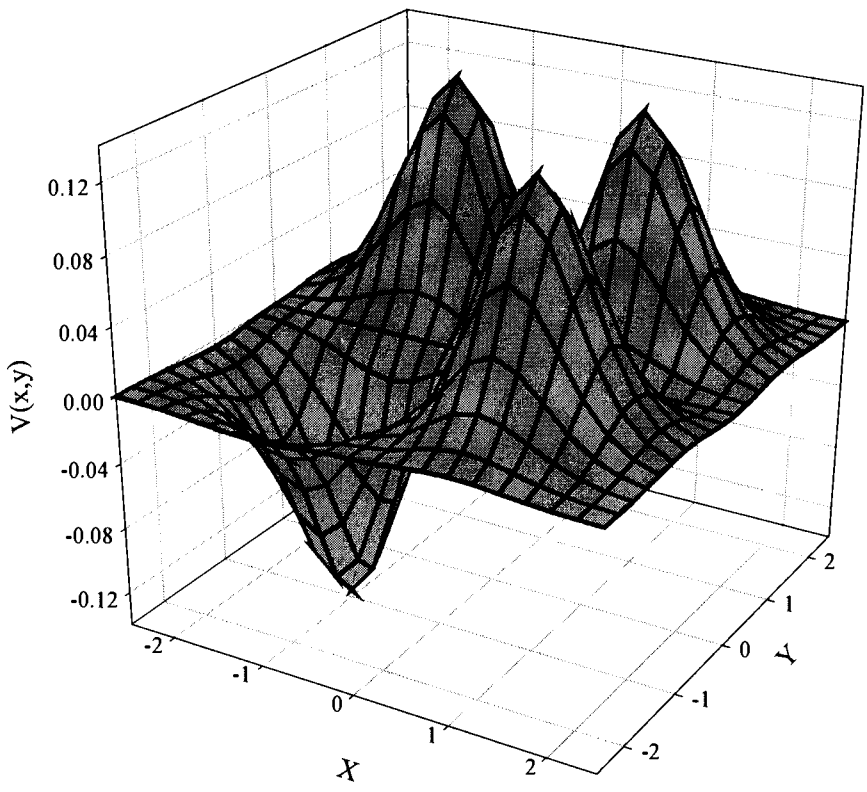

Figure 2.7 – Three-dimensional mesh plot of V_{5A} (Equation 2.2-8)

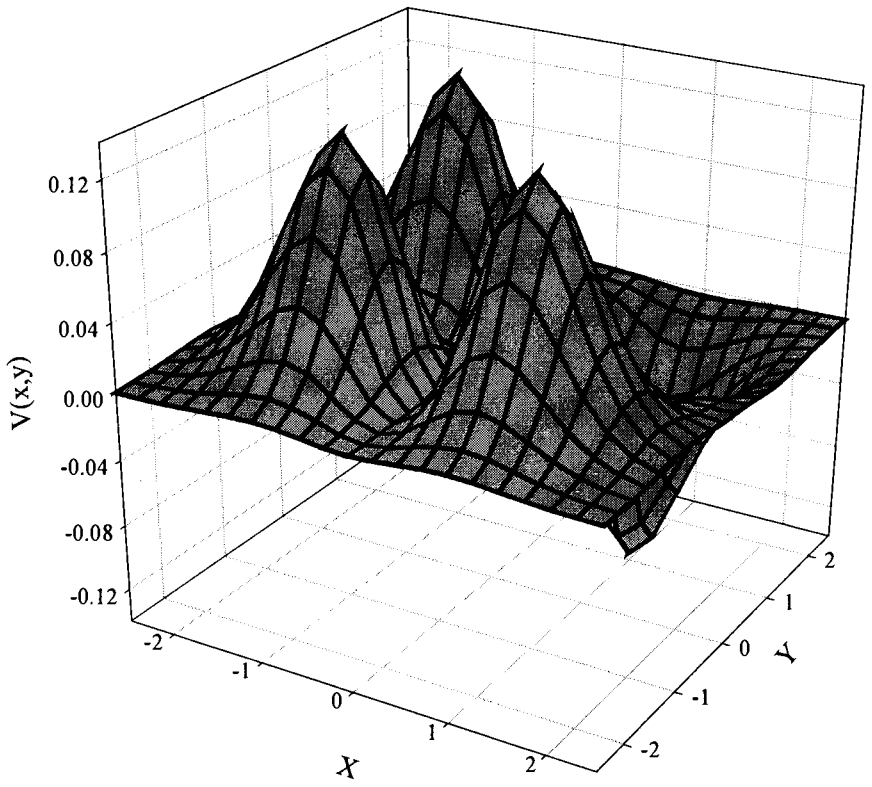

Figure 2.8 – Three-dimensional mesh plot of V_{5B} (Equation 2.2-9).

The last potential studied was the negative of V_1 and was the only potential with four negative hills:

$$V_6(x,y) = -x^2y^2e^{-(x^2+y^2)} \qquad [2.2\text{-}10]$$

The mesh plot for this potential is shown in the following figure.

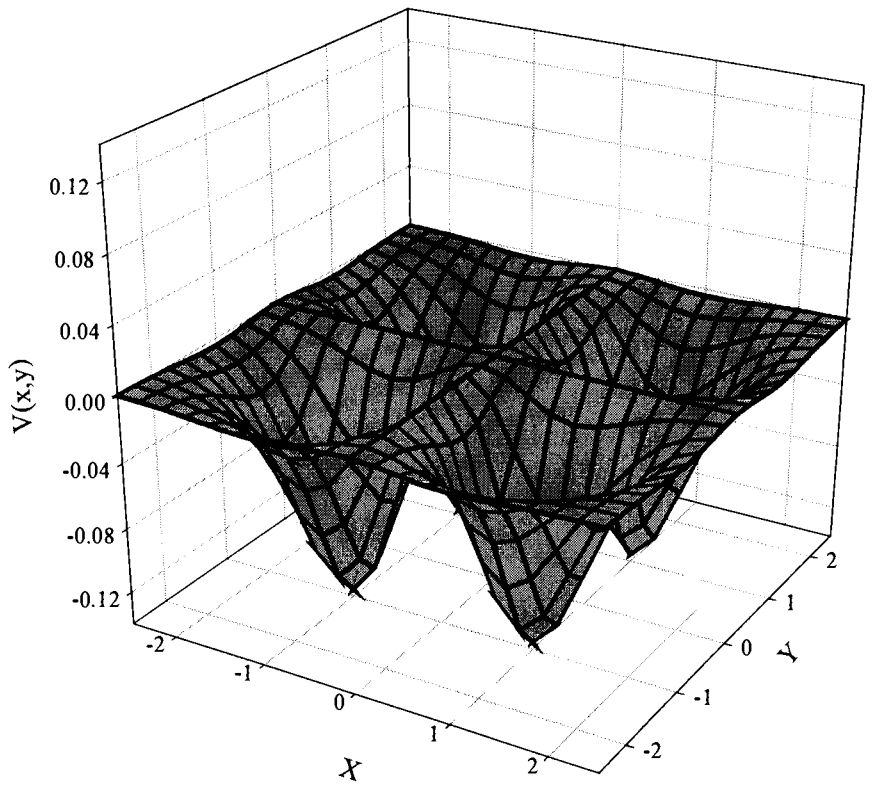

Figure 2.9 – Three-dimensional mesh plot of V_6 (Equation 2.2-10).

Some concern has been expressed about the sign function. This function does not have a continuous derivative around sign(x=0). Part of our motivation for factoring out V(x,y) in Equations 2.1-15a and 2.1-15b was to avoid this discontinuity becoming a problem. It should be noted, however, that σ_i is simply a constant (± 1). At x=0, sign(x) is defined by:

$$\text{sign}(0) \equiv 1 \qquad [2.2\text{-}11]$$

So if we are required to take a derivative of our potential functions, we can evaluate the constant afterwards.

While it was necessary to present the three-dimensional surfaces of all ten potentials, we needed an easier way to keep track of them. Table 2.1, below, gives a summary of all of the potential names and their respective σ_i values.

Table 2.1 – Summary of the switch value, σ_i, for $V(x,y) = x^2y^2e^{-(x^2+y^2)}\sigma_i$.

Potential	σ_i
V_1	sign(1)
V_{2A}	sign(-x)
V_{2B}	sign(x)
V_{2C}	sign(y)
V_3	sign(-xy)
V_{4A}	$\frac{-1-\text{sign}(x)+\text{sign}(y)-\text{sign}(xy)}{2}$
V_{4B}	$\frac{-1+\text{sign}(x)+\text{sign}(y)+\text{sign}(xy)}{2}$
V_{5A}	$-\frac{-1-\text{sign}(x)-\text{sign}(y)+\text{sign}(xy)}{2}$
V_{5B}	$-\frac{-1+\text{sign}(x)+\text{sign}(y)+\text{sign}(xy)}{2}$
V_6	sign(-1)

We simplified all of the Three-dimensional systems, visually, to a set of four hard spheres. The sign of the circle represent the sign of the potential hill in Figures 2.1-2.9.

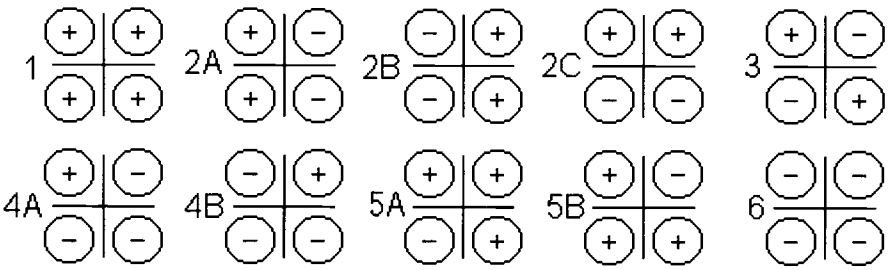

Figure 2.10 – Two-dimensional representations of Equations 2.2-1 through 2.2-10.

We have four hills, each of which can be either positive or negative. This leads to sixteen possible combinations ($2^4 = 16$). Of these sixteen potentials, only ten (the ones we used) are unique after reflection across the x-axis. Because our particle comes in parallel to the x-axis, we could discard the six potentials that weren't unique.

Between Equations 2.1-15a and 2.1-15b and the σ_i provided in Table 2.1, we had everything we needed to perform our scattering experiments. In the next section, Section 3, we go into the details and theory of quantifying chaos.

3. CHARACTERIZING CHAOS

This section focuses on the theoretical details of chaotic scattering. This includes discussions about phase space, manifolds, bifurcations, and the topological changes that result in chaos. We also examine two ways of characterizing a chaotic system qualitatively: through geometry and dynamics (time dependent behavior). The concept of fractal dimension, in particular capacity dimension, is used to characterize the system's geometry. On the other hand, we use the Lyapunov exponent to measure the dynamic behavior of the system. While these are not the only ways to characterize chaos, they are two of the most useful and fundamental.

3.1. TOPOLOGY OF CHAOS

3.1.1. Spaces

The concept of space and degrees of freedom is often filled with contradictory definitions. For a Hamiltonian system, however, things are a little clearer. The number of momentum coordinates is the number of degrees of freedom. For our system, we have two degrees of freedom and a two dimensional scattering space (12).

Since we have a total of four variables in the Hamiltonian equations, p_x, p_y, x, and y, we have a four-dimensional phase space. Since energy is conserved and the momentum coordinates (p_x and p_y) are related, we only have three independent variables. Therefore, the trajectories travel inside phase space along a three-dimensional energy surface called energy space (13). In studying this energy surface, we are able to understand the causes and types of chaos.

3.1.2. Manifolds, sets, and chaotic saddles

To understand where chaos occurs in the scattering system, we need to start by examining the fixed points of the system. A fixed point is a place, in phase space, that does not change with time. In other words, the time derivative is zero. It is simple to reduce the two 2nd order differential equations into four 1st order differential equations. The details of this will be presented in Section 4.1. For now we will simply use the results:

$$\frac{dz_0}{dt} = z_2 \qquad [3.1\text{-}1a]$$

$$\frac{dz_1}{dt} = z_3 \qquad [3.1\text{-}1b]$$

$$\frac{dz_2}{dt} = \frac{2}{m}\left(\frac{1}{z_0} - z_0\right)V(z_0, z_1) \qquad [3.1\text{-}1c]$$

$$\frac{dz_3}{dt} = \frac{2}{m}\left(\frac{1}{z_1} - z_1\right)V(z_0, z_1) \qquad [3.1\text{-}1d]$$

where $z_0 = x$, $z_1 = y$, $z_2 = dx/dt$, $z_3 = dy/dt$, and V is our potential.

To find the fixed points in our system, we set each of the time derivatives equal to zero and solve the resulting equations:

$$z_2 = 0 \qquad [3.1\text{-}2a]$$

$$z_3 = 0 \qquad [3.1\text{-}2b]$$

$$\frac{2}{m}\left(\frac{1}{z_0} - z_0\right)V(z_0, z_1) = 0 \qquad [3.1\text{-}2c]$$

$$\frac{2}{m}\left(\frac{1}{z_1} - z_1\right)V(z_0, z_1) = 0 \qquad [3.1\text{-}2d]$$

Equations 3.1-2a and 3.1-2b represent the case where the particle has no velocity in either the x or the y direction.

We are going to start by looking for a fixed point in the spatial coordinates, x and y. Equations 3.1-2a and 3.1-2b do not include either of the spatial variables, so it is best to focus on Equations 3.1-2c and 3.1-2d. We convert these equations back into terms of x and y and substitute in the generalized form of the potential from Equation 2.1-11, $V(x,y) = x^2y^2e^{-(x^2+y^2)}\sigma_i$.

$$\frac{2}{m}\left(\frac{1}{x} - x\right)x^2y^2e^{-(x^2+y^2)}\sigma_i = 0 \qquad [3.1\text{-}3a]$$

$$\frac{2}{m}\left(\frac{1}{y} - y\right)x^2y^2e^{-(x^2+y^2)}\sigma_i = 0 \qquad [3.1\text{-}3b]$$

The solutions to these two equations give the following x and y coordinates: (1,1), (-1,1), (1,-1), (-1,-1), and (0,0) for the fixed points in our system. Note that these fixed points coincide exactly with the center of our potentials hills in each quadrant. In addition, the x-axis and y-axis are also fixed points, but are not of experimental interest. If the particle is incident along the axes themselves, it will simply pass directly through the system. Since the solutions to Equations 3.1-3a and 3.1-3b are independent of σ_i, they are independent of the specific potential system

If the fixed point were on a positive hill, it would obviously be an unstable point. It is also unstable on a negative hill, because the particle has positive energy, so it will simply skip out of the potential well. The origin (0,0) could not be stable because the four different potential hills around it would attract or repel the particle away. From this we conclude that all of the fixed points in the system are unstable.

We will show in Section 3.3.2 that we have one direction of expansion and one direction of contraction (14). If we look at a plane in our three-dimensional energy surface, we have a simple two-dimensional system. A representation of this is shown in Figure 3.1.

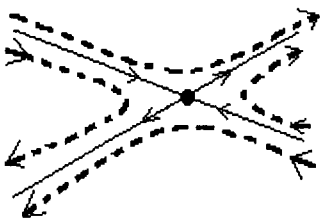

Figure 3.1 – Schematic of one of the five fixed points in our scattering problem. Dashed lines are typical trajectories approaching the fixed point.

This type of fixed point is called a saddle point as will be shown shortly. Note that only points that are exactly on the contracting direction will reach the fixed point. We now expand into the third dimension of the energy surface:

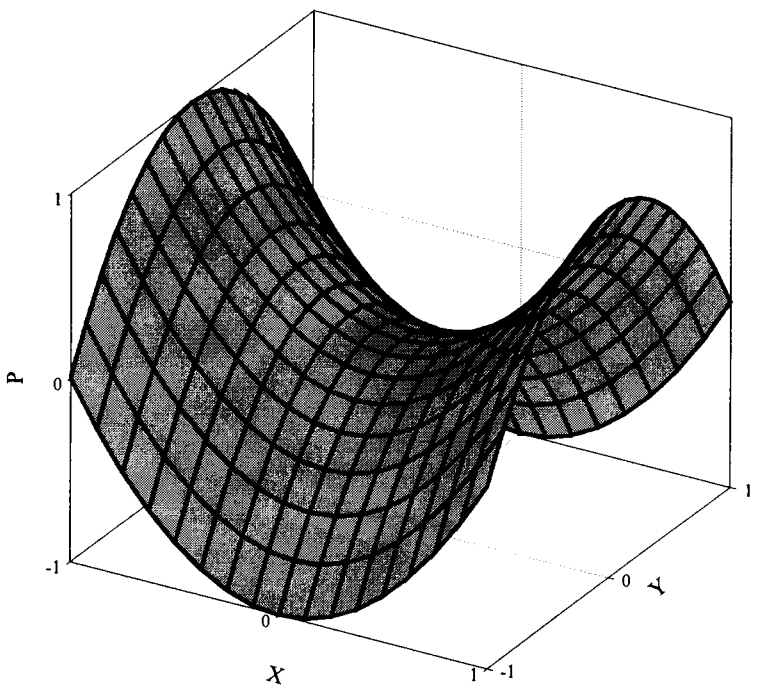

Figure 3.2 – Three-dimensional schematic of one the five fixed points in our system.

Since the shape of Figure 3.2 looks a bit like a saddle, the fixed point is called a saddle point.

Now we begin to divide up our energy space. All trajectories that directly approach a saddle point, P_k, are called the stable manifold, SM_k. The unstable manifold, UM_k, contains all trajectories that leave directly from saddle point P_k. All the trajectories that are in the unstable or the stable manifold, of P_k form the invariant manifold, IM_k (also known as the invariant set). The manifolds have a highly complicated geometrical structure that we refer to as a fractal. We will be discussing fractals and how they are measured in the next subsection, Section 3.2.

Neither the stable manifold nor the unstable manifold, *of the same fixed point,* may cross itself. It is possible, for a stable and unstable manifold to intersect, if they become tangent to each other. When these two manifolds come from the same fixed point, it is called a homoclinic intersection. If the intersecting manifolds originate from different fixed points, they are called heteroclinic intersections.

The chaotic set, which is nonattractive, (also called a strange saddle) is made up of these intersections between the stable and unstable manifolds. Since these manifolds are fractal, the chaotic set is so as well. It is the characteristics of this set that determine how a particle interacts with the scattering region. Despite the unboundedness of scattering trajectories in both spatial space and phase space (the particle exits to infinity), the chaotic set is still bounded (15).

We consider the motion of a scattering trajectory that starts close to the stable manifold of P_1. At first, it will be attracted along the path of SM_1. After staying there for some time it will be repelled away along UM_1. At this point the trajectory can either exit off to infinity along UM_1, or it can visit another stable manifold ($SM_{i\neq1}$) via a heteroclinic intersection (or SM_1 by a homoclinic intersection). At a later time, it will either exit to infinity or find another way back to a stable manifold. Eventually, it will exit the scattering region and escape to

infinity. Trajectories that remain in the system longer, and thus have a longer delay time, are closer to becoming trapped by the system. It is this almost trapping of orbits that leads to the chaotic nature of scattering data (16).

The dynamical origin of chaotic scattering originates from a chaotic set (nonattractive) in energy space that containing an infinite number of unstable periodic and aperiodic orbits (not manifolds). A trajectory coming into the scattering region typically spends a finite amount of time near the chaotic set before exiting the scattering region to infinity. Staying near the set gives rise to the chaotic nature of the scattering process. The infinite number of unstable (almost) periodic orbits embedded in the chaotic set leads to the infinite number of singularities in the scattering function (Section 5) (3).

3.1.3. Bifurcation and types of scattering

In the previous subsection, Section 3.1.2, we discussed the chaotic set. When the behavior of the system changes character, at a specific value of a system parameter (energy in our case), this is called a bifurcation. The change is due to a change in structure of the chaotic set (17).

In a generic chaotic scattering experiment, the system has regular behavior (i.e. nonchaotic) for energies above a critical energy, $E>E_c$. For energies lower than the critical energy, the system displays chaotic behavior in the scattering functions. The type of bifurcation is classified based upon how the chaotic set changes on either side of this bifurcation energy.

There are two major routes to chaotic scattering: Saddle centre bifurcation and abrupt bifurcation. The difference between these two lie in the structure of the chaotic set before the bifurcation energy.

In the saddle centre bifurcation, the chaotic set exists at all energies. There exists a bounded chaotic region in the phase space surrounded by classically

forbidden potential barriers. The bounded chaos is typically developed through the destruction of a collection of Kol'mogorov-Arnol'd-Moser (KAM) tori. KAM tori can be thought of as structures in phase space that prevent the particle from freely traveling throughout a region (even if they are not classically forbidden). The KAM tori keep the particle from interacting with the chaotic set, so the dynamics are regular. At the critical energy, E_c, the tori dissolve allowing the particle access to the chaotic set (18).

In contrast to the saddle centre bifurcation, the chaotic set in an abrupt bifurcation does not exist until the critical energy. Then, the chaotic set comes entirely into existence (thus calling it abrupt). Also, there are no KAM tori, so the particle can access all parts of the system that are not classically forbidden (9).

Within the abrupt bifurcation class, there are a number of subclasses (besides the generic route). We will be focusing on the three main types: crisis, massive, and nonhyperbolic.

If two or more of the saddle points collide, through a complicated sequence of intersection in their stable and unstable manifolds, it is referred to as a crisis in chaotic scattering. Chaotic scattering is generally enhanced throughout the crisis as an infinite number of new scattering trajectories become possible (19).

Another example of abrupt bifurcation is massive bifurcation. The massive bifurcation destroys all the unstable periodic orbits, and simultaneously replaces them with a new set (20).

Finally, there is nonhyperbolic abrupt bifurcation. In this type of scattering, the chaotic set appears suddenly (like generic abrupt bifurcation), but not all regions are accessible because of KAM tori. These KAM tori dissolve as the energy parameter is changed, allowing the particle access to more of the chaotic set (10). While both this bifurcation and saddle-centre bifurcations contain KAM tori, the chaotic set is different. For nonhyperbolic abrupt bifurcation, the chaotic set suddenly comes into existence at the critical energy, but in saddle-centre bifurcation the chaotic set exists at all energies.

By measuring properties of the chaotic set, it is possible to tell the difference between saddle centre bifurcation and abrupt bifurcation. It is also possible to tell the subclasses of abrupt bifurcation apart. We will discuss this further in Section 3.2.

3.2. GEOMETRIC CHARACTERIZATION

3.2.1. Fractals

We stated earlier that the stable manifold, unstable manifold, invariant manifold, and chaotic set have a fractal dimension (and are thus fractals). Dimension, in general, can be thought of as a measurement of how much volume a curve (of any dimensions) occupies.

This is easier to understand with an example. We start with a line, a box, and a cube. First, we divide its linear size into equal lengths, L, in each spatial direction (one direction for a line, two for a square, and three for a cube). Note that each of the boxes are "self-similar" to the original (they have the same shape). We then count the number of "boxes", N(L), present. This methodology is shown in Figure 3.3.

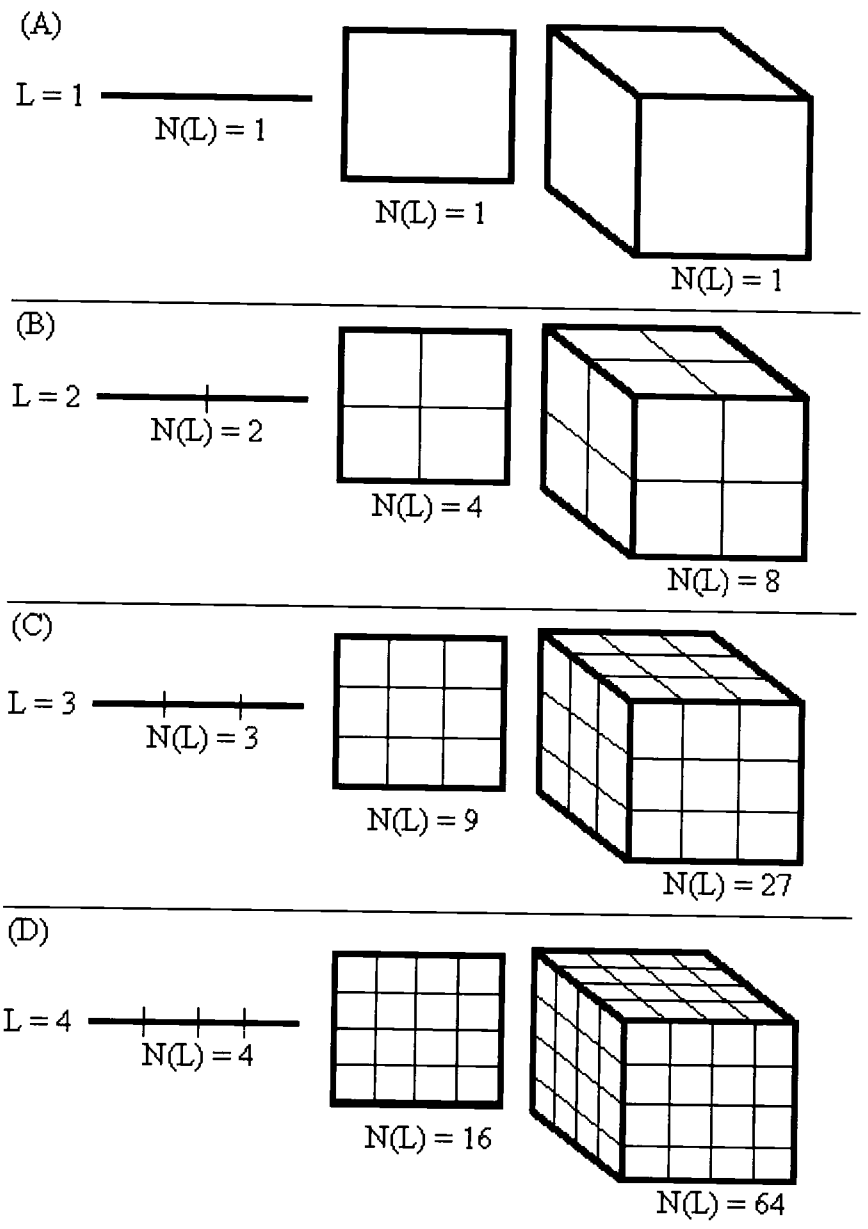

Figure 3.3 – Dividing common objects along their edge into, equal lengths of size (A) L=1 (B) L=2 (C) L=3 (D) L=4, and counting the number of boxes, N(L).

Now we are looking for a relationship between L and N(L). It is obvious that as we divide the edge into smaller pieces, by increasing L, we increase the

number of boxes inside the object, N(L). The only equation that fits all of the possibilities is:

$$N(L) = L^{D_b} \qquad [3.2\text{-}1]$$

where D_b is the dimension of the object. The subscript, b, is added as a reminder that the value as found using boxes. This is often called the box counting dimension. We solve the above equation for D_b:

$$D_b = \lim_{L \to \infty} \frac{\ln N(L)}{\ln L} \qquad [3.2\text{-}2]$$

The limit, which divides up the sides into an infinite number of equal lengths, was added in preparation of discussing more complex shapes than those presented above. This is the basic definition of dimension that we will be using. Note that we find that $D_b = 1$ for the line, $D_b = 2$ for the box, and $D_b = 3$ for the cube. These are the expected Euclidian dimensions. While the Euclidian dimensions are integers, a fractal is defined as having a non-integer dimension value. Fractals are self-similar (just like the boxes above), or nearly so, on many different scales.

Fractal dimension is an incredibly powerful tool. It allows us to resolve the difference between highly complicated structure and random noise. We will use this tool extensively in the next subsection.

3.2.2. Capacity dimension

Section 3.1 showed that the structure of the chaotic set is very important for explaining and predicting chaotic scattering. Now we will use the idea of fractal

dimension to characterize the geometric properties of the chaotic set, and the stable and unstable manifold. The fractal dimension used is assumed to be the box counting dimension discussed earlier. These equations and discussion follow from a paper (21) on higher dimensional fractal structure that has been reduced to fit our system.

The chaotic set is defined to be the intersection of the stable and unstable manifold. We can relate the fractal dimension of this set to the fractal dimension of its stable and unstable manifold by:

$$D_c = D_u + D_s - M \qquad [3.2\text{-}1]$$

where D_c is the fractal dimension of the chaotic set, D_u is the fractal dimension of the unstable manifold, D_s is the fractal dimension for the stable manifold, and M is the degrees of freedom in energy space. For our system $M = 2N - 1 = 3$.

We have a Hamiltonian system that is an even function of the momentum vectors, and the position vectors can be evolved backwards in time, therefore the system is time reversible. We then expect the stable and unstable manifolds to have the same dimension:

$$D_u = D_s \qquad [3.2\text{-}2]$$

We showed earlier that chaotic scattering is a result of orbits becoming almost trapped inside the potential. Trajectories that start out close to the stable manifold stay trapped the longest. A typical scattering experiment will vary the impact parameter, b, over a large region and measure output characteristics. The intersection of this one-dimensional parameter space, b, with the stable manifold, gives rise to the singularities in the scattering data. It is possible to find the fractal

dimension of this intersection, d_I, using a technique that will be presented in Section 4. d_I is also known as the capacity dimension.

It will be shown shortly that finding the capacity dimension will completely characterize the basic geometric properties of the chaotic set. However, it is important to realize that if $d_I = 0$, the parameter space and the stable manifold do not intersect. If this happens, the system will not have any trajectories that spend an inordinate amount of time in the system. Therefore, the scattering data will not contain singularities. It is possible to relate the dimension of the stable manifold to d_I:

$$D_S = d_I + N \qquad [3.2\text{-}3]$$

where N is the number of degrees of freedom in the system (two for our system). Combining this equation with Equations 3.2-1 and 3.2-2 yield:

$$D_C = 2d_I + 1 \qquad [3.2\text{-}4]$$

where we have substituted M=3 and N=2 into the equation. Thus, measurement of the capacity dimension characterizes the stable and unstable manifolds and the chaotic set.

Special mention needs to be made of the case when d_I=0. As mentioned previously, this indicates that the parameter space and the stable manifold no longer intersect. Using Equation 3.2-3, we see that the stable manifold reduces to a plane in energy space. Since that stable and unstable manifold have equal dimension, the unstable manifold becomes a plane as well. However, it is important to realize that the parameter space still intersects the unstable manifold. While the stable and unstable manifold have the same shape, they do not have to be orientated the same in energy space (21).

Now we address the issue of differentiating the types of bifurcations mentioned in Section 3.1 by their geometric properties. We will start with the saddle centre bifurcation.

The saddle centre bifurcation occurs as a chaotic saddle is gradually formed due to dissolving of the KAM tori. This gradual onset of chaos manifests itself in the capacity dimension. The capacity dimension will start at a non-zero value (because the chaotic set was already in existence) and then rise to unity as the system parameters are changed (22).

In the generic abrupt bifurcations, the chaotic set is suddenly created. So any value above the critical energy will have no intersections between the parameter space and the stable manifolds. Thus d_l will be equal to zero both above and exactly at the critical energy. In fact it has been shown (9) for this type of abrupt bifurcation that the capacity dimension scales with energy as:

$$d_l \propto \frac{1}{\ln\left(\frac{1}{E_c - E}\right)} \qquad [3.2\text{-}5]$$

where E_c is the critical energy.

A crisis type of bifurcation results when the system has two or more saddle points which collide as energy changes. The system will transition through a discrete number of these collisions as the energy is changed. The chaotic set is constant until the next crisis occurs. Because of this, the fractal dimension will also be constant until another crisis. This results in a structure that has been referred to as a "devil's staircase", where the capacity dimension will suddenly jump to a new larger constant at the onset of crisis (remaining there until the next one) (23).

A massive bifurcation results when the entire chaotic set is destroyed and then immediately recreates the chaotic set. Where the generic and crisis type of abrupt bifurcations have a regular pattern, the massive bifurcation will have an

almost random pattern. This randomness comes with the continuous creation and destruction of fixed points (24).

Nonhyperbolic abrupt bifurcations occur when the energy surface contains a chaotic set that suddenly appears, but still has KAM tori that block a particle from getting to it. The key difference between this bifurcation and the generic abrupt bifurcation is the *discontinuous* change in capacity dimension. This happens because of a sudden access of scattering particles to an already developed chaotic set. The capacity dimension will rise, often slowly, to a value that is less than unity. This is in contrast to the saddle-centre bifurcation that reaches unity eventually; giving a way to differentiate between the two bifurcations (3.3-6).

Using these characteristics, it is possible to characterize the size of the chaotic set and the route to chaos in the scattering system.

3.3. THE LYAPUNOV EXPONENT

This subsection delves into the dynamical and geometrical meaning of the Lyapunov exponent and Lyapunov characteristic exponent.

3.3.1. Lyapunov characteristic exponent

The geometric dimensions of Section 3.2 are quite useful for discovering details about the structure of phase space. However, they do not allow us to measure how chaotic the system is. For this, we must look at the dynamic properties of the system. We have stated many times that the mark of chaos is an extreme sensitivity upon initial conditions. Now we take that qualitative definition and try to make it quantitative.

We start with two trajectories that have the exact same initial conditions, but are separated by a distance of d_0 to start with. The two trajectories are evolved until a time, t, and the distance, d_t, is measured. The separation distance is assumed to be an exponential function of time. This leads to the formula for d_t:

$$d_t = d_0 e^{\lambda t} \qquad [3.3\text{-}1]$$

where λ is called the Lyapunov exponent. The size of the exponent will determine the rate of divergence (or convergence) of the two trajectories.

This exponent is often considered to be the most fundamental measure of chaos (25). If the exponent is negative, the trajectories eventually will converge back together. This indicates that the two trajectories are not in a chaotic region. A positive Lyapunov exponent means that the two trajectories diverge over time, indicating chaos in the region. In fact, any system that contains at least one positive Lyapunov exponent is defined to be chaotic. The magnitude of the exponent reflects the time scale on which system dynamics become unpredictable (26).

While Equation 3.3-1 is a good starting point for calculating λ, many properties of the Lyapunov exponent become clear with more formal treatment. The following discussion parallels the discussion of References (1) and (27). Our goal is show how the trajectory changes in each dimension of phase space. This is done using the Lyapunov characteristic exponent (LCE).

We start with initial points, x_0 and x, separated by a small distance d_0. Let $x_0(t)$ be the trajectory resulting from starting point x_0 and x(t) be the trajectory from x. For simplicity, the system has a single development equation:

$$\frac{dx(t)}{dt} = f(x(t)) \qquad [3.3\text{-}2]$$

The distance between these two trajectories is simply:

$$d_t = x(t) - x_0(t) \qquad [3.3\text{-}3]$$

and the rate of change between these two trajectories is given by:

$$\frac{d(d_t)}{dt} = \frac{dx(t)}{dt} - \frac{dx_0(t)}{dt} = f(x(t)) - f(x_0(t)) \qquad [3.3\text{-}4]$$

For reasons that will become apparent shortly, we perform a Taylor expansion of f(x(t)). Since we have assumed that the points, x_0 and x, are close together:

$$f(x(t)) = f(x_0(t)) + (x(t) - x_0(t))\left.\frac{df(x(t))}{dx}\right|_{x_0(t)} + \ldots \qquad [3.3\text{-}5]$$

where we have dropped the higher order terms. Combining this equation with Equation 3.3-4, and dropping higher order terms yields:

$$\frac{d(d_t)}{dt} = (x(t) - x_0(t))\left.\frac{df(x(t))}{dx}\right|_{x_0(t)} \Rightarrow$$

$$\frac{d(d_t)}{dt} = d_t \left.\frac{df(x(t))}{dx}\right|_{x_0(t)} \qquad [3.3\text{-}6]$$

The second equation used the definition of the distance between the two trajectories given in Equation 3.3-3. We now relate this to the assumption that the divergence of the two trajectories is exponential in nature. So we take the derivative of Equation 3.3-1 to compare to the above equation:

$$\frac{d(d_t)}{dt} = \frac{d}{dt} d_0 \lambda e^{\lambda t} = d_0 \lambda e^{\lambda t} = d_t \lambda$$

$$\frac{d(d_t)}{dt} = d_t \lambda \qquad [3.3\text{-}7]$$

Direct comparison between Equation 3.3-6 and 3.3-7 leads to the definition for the Lyapunov exponent in terms of the derivative:

$$\lambda \equiv \left. \frac{df(x(t))}{dx} \right|_{x_0(t)} \qquad [3.3\text{-}8]$$

The value of this derivative will usually change with x and is a local exponent. To find a global exponent we average the exponent, at each point in time, over the whole trajectory.

For multidimensional systems, we associate a Lyapunov exponent with each coordinate direction. This is referred to as a Lyapunov characteristic exponent (LCE).

$$\lambda_i = \frac{\partial f_i}{\partial x_i} \qquad [3.3\text{-}9]$$

where f_i is the time function for coordinate x_i. This represents how a trajectory will expand or contract in this single coordinate. If one of the exponents is positive, then the system is considered chaotic. The above equation simply measures how fast trajectories diverge, with respect to a single phase space coordinate, and is a local measure of phase space chaos.

A more rigorous treatment of this problem can be found in Reference (28). The result and interpretation, however, is the same.

3.3.2. Application to a Hamiltonian scattering system

The previous section focused on measuring how a trajectory changes in a single phase space coordinate. We are now going to address the problem of calculating the Lyapunov exponent (not the Lyapunov characteristic exponent). By examining our specific open Hamiltonian system, we can reduce the problem to finding the largest exponent.

While the Lyapunov exponent is the main tool used to characterize the dynamic behavior of the system, it also has a geometric meaning. To show this, we look at how a group of points evolve in time. We start with a "cube" in the four-dimensional phase space of our scattering experiment. The cube has sides $s_1=s_2=s_3=s_4$ but with different characteristic exponents, λ_1, λ_2, λ_3, and λ_4 respectively, associated with them. We order the exponents such that $\lambda_1 \geq \lambda_2 \geq \lambda_3 \geq \lambda 4$. The volume of the cube would be:

$$V_0 = s_1 s_2 s_3 s_4 \qquad [3.3\text{-}10]$$

Using Equation 3.3-1, we are able to find the volume as a function of time:

$$V(t) = s_1 e^{\lambda_1 t} s_2 e^{\lambda_2 t} s_3 e^{\lambda_3 t} s_4 e^{\lambda_4 t} = s_1 s_2 s_3 s_4 e^{(\lambda_1+\lambda_2+\lambda_3+\lambda_4)t} \Rightarrow$$

$$V(t) = V_0 e^{(\lambda_1+\lambda_2+\lambda_3+\lambda_4)t} \qquad [3.3\text{-}11]$$

Since the Lyapunov characteristic exponents, λ_i, are not generally equal, the box will become distorted over time. Each side will stretch over time according to its Lyapunov exponent. Since λ_1 is the largest exponent, s_1 will be the side that stretches out the most. Eventually, this side will dominate the distortion.

To see how much the volume will change with time, we take a time derivative of Equation 3.3-11:

$$\frac{dV}{dt} = V_0 e^{(\lambda_1+\lambda_2+\lambda_3+\lambda_4)t}(\lambda_1+\lambda_2+\lambda_3+\lambda_4) = (\lambda_1+\lambda_2+\lambda_3+\lambda_4)V \Rightarrow$$

$$\frac{1}{V}\frac{dV}{dt} = \lambda_1+\lambda_2+\lambda_3+\lambda_4 \qquad [3.3\text{-}12]$$

The left hand side of this equation is called the divergence of V. In a Hamiltonian system, phase space volume is conserved (29), and thus the divergence of this volume is zero. We substitute this into Equation 3.3-12 and find a relationship between the exponents:

$$\lambda_1+\lambda_2+\lambda_3+\lambda_4 = 0 \qquad [3.3\text{-}12]$$

Previously, we showed that the four-dimension phase space could be reduced to a three-dimensional constant energy surface. This causes one of the Lyapunov character exponents to vanish. To reduce this further, we look at Equation 3.3-9. The Lyapunov characteristic exponents, λ_i, are an indication of how the system responds to a small change (perturbation) in a phase space coordinate (x_i). Any perturbations that are orthogonal to the energy surface are stable (30). This causes another exponent to vanish. With two of the exponents being equal to zero, Equation 3.3-12 simplifies to:

$$\lambda_1 = -\lambda_2 \qquad [3.3\text{-}13]$$

This means that there is one direction of expansion and one of contraction. Also note, that unless the two exponents are zero, there is always chaos in the system.

For large times ($t >> \lambda^{-1}$) the system's distortion will be dominated by the largest Lyapunov characteristic exponent.

This allows us to use the two spatial coordinates, rather than all four of the phase space coordinates, to calculate average instability of an orbit over time (31). We define the Lyapunov exponent to be a function of time:

$$\lambda(t) = \lim_{t\to\infty}\left(\lim_{d_0\to 0}\frac{d_t}{d_0}\right) \qquad [3.3\text{-}14]$$

where d_0 is the initial separation of the trajectories and d_t is the spatial distance (Euclidian norm) between the two trajectories at time t. The order of the limits cannot be reversed. The formula for distance is given for completeness:

$$d_t = \sqrt{(x_1 - x_2)^2 + (y_1 - y_2)^2} \qquad [3.3\text{-}15]$$

where (x_1,y_1) and (x_2,y_2) are the spatial coordinates for the two trajectories at time t.

In equation 3.3-14, the first limit ($t\to\infty$) needs some clarification. In a scattering experiment, the particle comes into the system from infinity, spends a finite time in the scattering region, and exits off to infinity. So by $t\to\infty$, we really mean $t\to t_{exit}$ (where t_{exit} is the time it takes to exit the scattering region).

4. METHODS

This section focuses on the methods used to collect the data that will be presented in Section 5. Included are the experimental setup of the scattering problem and the reduction of the two 2^{nd} order differential equations of motion to four 1^{st} order differential equation. The fractal dimension of the chaotic set was calculated using the uncertainty exponent technique. The Lyapunov exponent was calculated using a brute force method.

4.1. EXPERIMENTAL SETUP

For each of the ten potentials, we used the exact same experimental setup. The particle came in from infinity on the left side, interacted with the scattering region, and exited off to infinity. A schematic is in Figure 4.1.

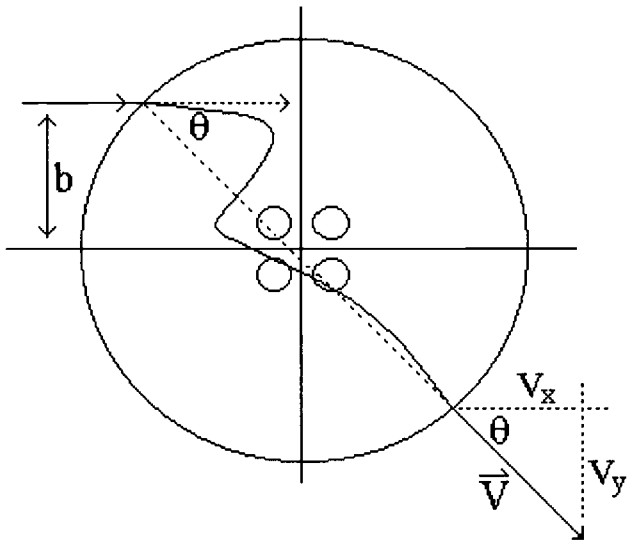

Figure 4.1 - Schematic of our scattering experiment where θ is the scattering angle and b is the impact parameter.

The area outside the circle represented the where the potential was zero and the distance was considered to be infinite. The dashed lines represented the particle's undeflected entry and exit paths. The angle formed by the intersection of these was defined to be the scattering angle. Because the particle was always incident parallel to the x-axis, the scattering angle was simply the angle of the exiting velocity vector:

$$\theta = \tan^{-1}\left(\frac{V_y}{V_x}\right) \qquad [4.1\text{-}1]$$

where V_x and V_y were the orthogonal components of the velocity vector.

Now we needed to be more precise about what we meant by "infinity". We defined infinity to be the distance at which the potential was approximately zero.

Since we only cared about the magnitude of the potential, we used the potential with four positive hills (V_1):

$$V_1(x,y) = x^2y^2e^{-(x^2+y^2)} \qquad [4.1\text{-}2]$$

We defined d_∞ to be the distance from the origin where $V(x,y) \approx 0$. The distance between a point (x,y) and the origin was given by:

$$d_\infty = \sqrt{x^2 + y^2} \qquad [4.1\text{-}3]$$

To pick a good value for d_∞ we solved the above equation for y, the substituted it into Equation 4.1-2.

$$V(x,\sqrt{d_\infty^2 - x^2}) = x^2\left(\sqrt{d_\infty^2 - x^2}\right)^2 e^{-\left(x^2+\left(\sqrt{d_\infty^2 - x^2}\right)^2\right)} \qquad [4.1\text{-}4]$$

which simplified to:

$$V(x,d_\infty) = x^2\left(d_\infty^2 - x^2\right)e^{-d_\infty^2} \qquad [4.1\text{-}5]$$

This equation gave the potential for all values of x that were a distance of d_∞ from the origin. As Equation 4.1-5 did not have a single exact solution, we used trial and error. Since the computer had a machine precision on the order of 10^{-16}, a d_∞ with a maximum potential of 10^{-25}, for all x, would be more than small enough.

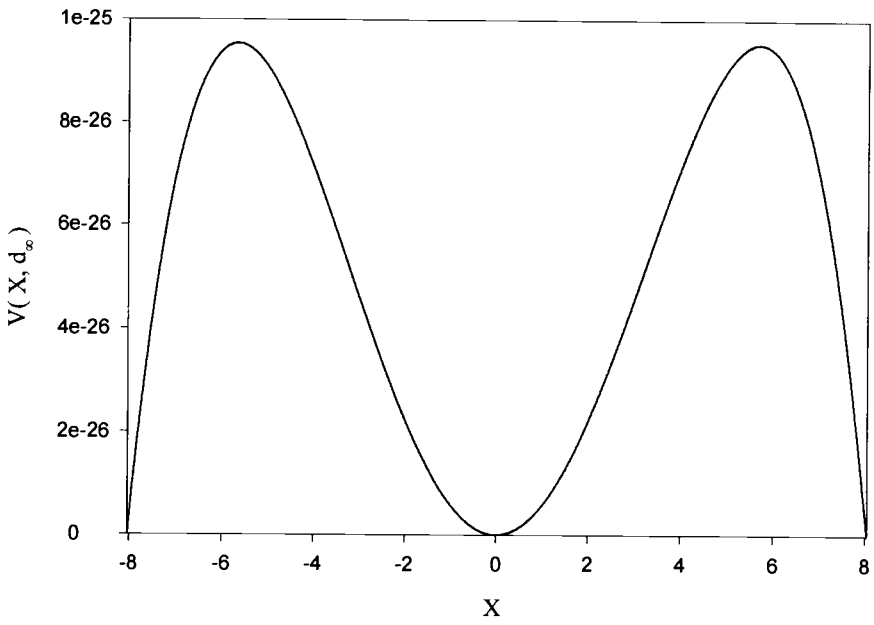

Figure 4.2 – Potential for all x values at a distance of 8.035 from the origin. From Equation 4.1-5 with $d_\infty = 8.035$.

Thus for our work, we defined infinity to be a distance of $d_\infty = 8.035$ from the origin.

4.2. NUMERICAL INTEGRATION

We used a standard 4^{th} order Runge-Kutta routine with fixed time step, τ, and no extrapolation. To use this RK4 solver, needed to reduce Equations 2.1-15a

and 2.1-15b to first order differential equations. This is accomplished by making the following substitutions:

$$z_0 = x \qquad [4.2\text{-}1a]$$

$$z_1 = y \qquad [4.2\text{-}1b]$$

$$z_2 = \frac{dx}{dt} \qquad [4.2\text{-}1c]$$

$$z_3 = \frac{dy}{dt} \qquad [4.2\text{-}1d]$$

which reduced to system to:

$$\frac{dz_0}{dt} = \frac{dx}{dt} = z_2 \qquad [4.2\text{-}2a]$$

$$\frac{dz_1}{dt} = \frac{dy}{dt} = z_3 \qquad [4.2\text{-}2b]$$

$$\frac{dz_2}{dt} = \frac{d^2x}{dt^2} = \frac{2}{m}\left(\frac{1}{z_0} - z_0\right)V(z_0, z_1) \qquad [4.2\text{-}2c]$$

$$\frac{dz_3}{dt} = \frac{d^2y}{dt^2} = \frac{2}{m}\left(\frac{1}{z_1} - z_1\right)V(z_0, z_1) \qquad [4.2\text{-}2d]$$

4.3. CAPACITY DIMENSION CALCULATION

In Section 3.2 we discussed the theory and meaning of the capacity dimension. It was on of the most important quantities in our scattering system. To find it we used a technique called the uncertainty exponent method. The assumption was that if two particles start out separated by a small distance of ε, yet exit

differently, then these two trajectories are either on different sides of the same stable manifold or different stable manifolds entirely. These two trajectories were considered uncertain to a value of ε. By measuring the probability that the two trajectories would exit opposite from our system, we measured the capacity dimension by:

$$P(\varepsilon) = \frac{N(\varepsilon)_{uncertain}}{N_{total}} = k\varepsilon^{1-d_1} \qquad [4.3\text{-}1]$$

where k was a proportionality constant, ε the initial separation, and d_1 the capacity dimension. We solved for the exponent in Equation 4.3-1 by taking the logarithm of both sides:

$$\ln(P(\varepsilon)) = \ln\left(k\varepsilon^{1-d_1}\right) \Rightarrow$$
$$\ln(P(\varepsilon)) = \ln(k) + (1-d_1)\ln(\varepsilon) \qquad [4.3\text{-}2]$$

This equation was the method by which we found the capacity dimension (9). We chose a large number (more on this shortly) of random trajectory pairs separated by ε_i, and calculated the probability that the trajectory pair would be uncertain, $P_i(\varepsilon_i)$. This was repeated for several values of ε_i. Then the $\ln(P_i(\varepsilon_i))$ was plotted as a function of $\ln(\varepsilon_i)$, as indicated in Equation 4.3-2. The slope of this line was denoted as α and d_1 was calculated by:

$$d_1 = 1 - \alpha \qquad [4.3\text{-}3]$$

The uncertainty exponent method is summarized in Table 4.1, below:

Table 4.1 – Algorithm for using the uncertainty exponent method to calculate capacity dimension.

Step	Action
1	Choose a random impact parameter (b).
2	Start with two trajectories with that have impact parameters b, and b±ε (the sign is chosen at random). All other initial conditions are identical.
3	Integrate the two trajectories using the RK4 ODE solver until both have exited the system.
4	If they exit opposite, the orbit is considered uncertain at that value of ε.
5	Repeat steps 1 through 4 a large number of times.
6	Count up the number of uncertain orbits.
7	Calculate the uncertainty probability, P(ε) at this value of ε, using Equation 4.3-1.
8	Repeat steps 1 through 7 for multiple values of ε.
9	Plot ln(P(ε)) as a function of ln(ε) and find the slope α.
10	Calculate the capacity dimension using $d_1 = 1 - \alpha$.

The only difficulty in applying this method was choosing how many total trajectory pairs, N_{total}, to use for each ε. For accurate results we required a reasonable amount of uncertain trajectories. For small ε enough, the number of

uncertain trajectories was roughly a constant. The total number of initial trajectories, N_{total}, needed was:

$$N_{total} = \frac{N(\varepsilon)_{uncertain}}{k\varepsilon^{d_1 - 1}} \propto \frac{1}{\varepsilon^{d_1 - 1}} \Rightarrow$$

$$N_{total} \propto \varepsilon^{d_1 - 1} \qquad [4.3\text{-}4]$$

So when $d_1 \approx 0$ (i.e. when there were almost no trapped orbits), the total number of trajectories required became very large (approximately 10^8 to 10^7). However, for d_1 closer to unity, fewer trajectories were required (10^4 to 10^6) (4.3-2).

Because we had no advanced knowledge of the capacity dimension value, and no common method was available in the literature, we standardized way to determine if more trajectories were needed. For our experiment we used a total of 10 values for ε: $10^{-3.5}$, 10^{-4}, $10^{-4.5}$, 10^{-5}, $10^{-5.5}$, 10^{-6}, $10^{-6.5}$, 10^{-7}, $10^{-7.5}$, and 10^{-8}. For each of these values of ε, we measured $P(\varepsilon)$ and fit the data to Equation 4.3-2. The regression statistics of this fit proved useful.

We used three different tests before accepting a capacity dimension result. First, we checked the correlation coefficient of, R^2, and rejected any results that had an $R^2 \leq 99.5\%$. Next, fits were made using all of the $P(\varepsilon)$ data (ten points), then the first nine points, then the first eight points, and so on until only the first three data points were being used. This allowed us the check the stability of our fits over various ranges. If these fits all passed the $R^2 > 99.5\%$ test and were within the error bounds of each other, we added the number of uncertain trajectories from another 20,000 starting trajectories to the data. If this did not change the capacity dimension, we concluded that we had a large enough sample for the starting trajectories. The capacity dimension was then taken to as the result from using the full set of data.

In Section 3.2.2, Equation 3.2-5, we discussed a scaling relationship between energy and capacity dimension for V_1 potential (Equation 1.3-1):

$$d_1 = \frac{k}{\ln\left(\frac{1}{E_c - E}\right)} \qquad [4.3\text{-}5]$$

where k was a proportionality constant, d_1 was the capacity dimension, and E_c was the critical energy. For each potential, we fitted our capacity dimension results to this Equation.

4.4. LYAPUNOV EXPONENT CALCULATION

The Lyapunov exponent is a dynamic (time dependent) measurement of the divergence of near-by trajectories. It is the most fundamental measure and indication of chaos in a system. A larger Lyapunov exponent corresponds to a more chaotic system (2).

While there were a number of commonly used methods to find the exponent (32, 33, 34, 35, 36), we used a brute force method to find the Lyapunov exponent. We started with Equation 3.3-1:

$$d_t = d_0 e^{\lambda t} \qquad [4.4\text{-}1]$$

where d_t was the separation between two trajectories at time t, d_0 was the initial

separation, and λ was the Lyapunov exponent. We then took the natural logarithm of both sides:

$$\ln(d_t) = t\lambda + \ln(d_0) \qquad [4.4\text{-}2]$$

We found, using scattering function data, where the scattering region was located. Then plotted $\ln(d_t)$ as a function of t, and took the slope to be Lyapunov exponent. A simple linear regression gave us λ. If the regression did not fit very well (low R^2 value), then we concluded that the particle was not behaving chaotic.

This approach had been called the "naive" approach. The naiveté comes in failing to realize that the calculated exponent was dependent upon a wide range of variables (4.3-6). The largest factors were the initial separation, d_0, between the two trajectories and the time step, τ, used by the RK4 ODE solver itself.

We start with two trajectories, TJ_{b1} and TJ_{b2}, with starting impact parameters b_1 and b_2, separated by a distance of $d_0 = \delta b$. They both have identical velocities and starting x values. We let a point, $p_b(t)$, be the x and y coordinate of a trajectory with starting impact parameter b at some time, t:

$$p_b(t) = [x(t),y(t)] \qquad [4.4\text{-}3]$$

We were not interested in the whole trajectory region, but the part of it that was inside the chaotic scattering region. We defined a subset of TJ_{b1} and TJ_{b2} where both trajectories were inside the scattering region. We called the smallest time when both trajectories were inside the scattering region as t_0 and the largest time as

t_{exit}. We were then able to define the two trajectories, T_{b1} and T_{b2}, using Equation 4.4-3 and the times t_0 and t_{exit}:

$$T_{b1} = \{p_{b1}(t_0), p_{b1}(t_1), ..., p_{b1}(t_{exit})\} \quad [4.4\text{-}4a]$$

$$T_{b2} = \{p_{b2}(t_0), p_{b2}(t_1), ..., p_{b2}(t_{exit})\} \quad [4.4\text{-}4b]$$

It was these subsets that were used to calculate the Lyapunov exponents. Once a particle exits the scattering region, it would never return. This was found analytically by tracking individual trajectories. The impact parameters that result in a trajectory entering R were called the impact region. These two regions are defined in Table 4.2.

Table 4.2 – Scattering region and impact region for the different potentials.

	Scattering Region		Impact Region
	x	y	b
V_1	-1 to 1	-1 to 1	-1.2 to 1.2
V_{2A}	-1 to 1	-1 to 1	-1.2 to 1.2
V_{2B}	-1.2 to 1	-1.2 to 1.2	-3 to 3
V_{2C}	-1.2 to 1.2	-1.2 to 1	-3 to 1
V_3	-1.2 to 1	-1.2 to 1	-3 to 1
V_{4A}	-1.2 to 1	-1.2 to 1	-3 to 1
V_{4B}	-1.2 to 1.2	-1.2 to 1.2	-3 to 3
V_{5A}	-1.2 to 1	-1.2 to 1	-3 to 1
V_{5B}	-1 to 1	-1 to 1	-1.2 to 1.2
V_6	-1.2 to 1.2	-1.2 to 1.2	-3 to 3

We defined d_t, separation distance at time t, in terms of our trajectory sets, T_{b1} and T_{b2}. At a time, $t_{exit} \geq t \geq t_0$, this distance was given by:

$$d_t = \|p_{b1}(t) - p_{b2}(t)\| = \sqrt{(x_1(t) - x_2(t))^2 + (y_1(t) - y_2(t))^2} \qquad [4.4\text{-}5]$$

To find a single Lyapunov exponent, we measured the distance between the two trajectories (as a function of time) while both were inside the chaotic scattering region. A linear regression was performed and the slope taken to be λ, as indicated by Equation 4.4-2. The regression statistics were then used to accept or reject this value for the Lyapunov exponent. We kept values that had an $R^2 \geq 97\%$ and $\sigma_\lambda/\lambda \leq 5\%$. This criterion helped to eliminate trajectories that weren't chaotic.

We could now find a single Lyapunov exponent, but needed to deal with the dependence of λ upon the time step (τ) and the initial separation (δb). We fixed the value τ and δb (and energy E) and scanned over the impact region. The largest exponent was kept and called $\lambda_{max}(\delta b, \tau)$. We looked at a number of time steps and separations for V_1 (Equation 4.1-2) in Figure 4.3.

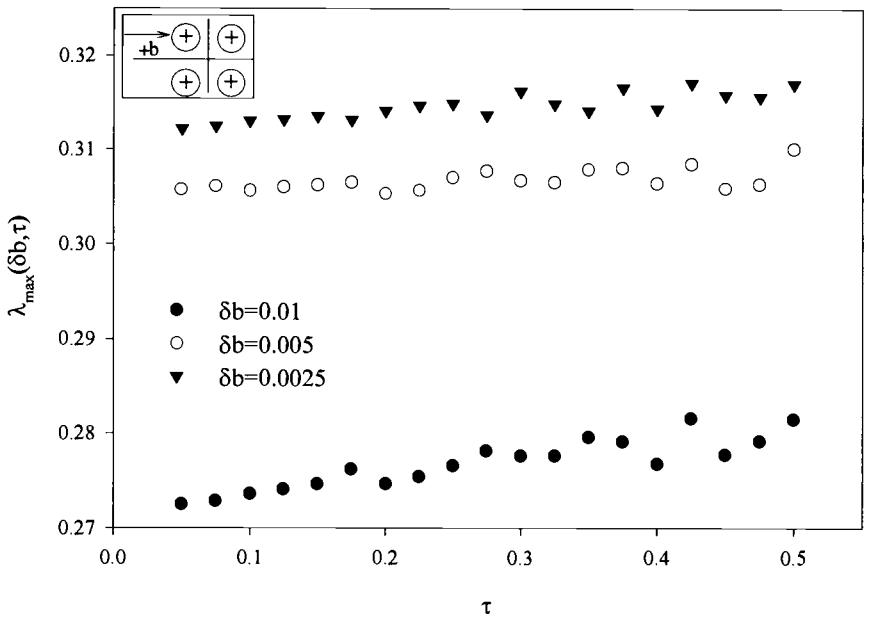

Figure 4.3 – $\lambda_{max}(\delta b, \tau)$ for different initial trajectory separation, δb, and ODE solver time step, τ, using V_1 and E=0.035.

From the above figure it was apparent that as $\tau \rightarrow 0$, the value of $\lambda_{max}(\delta b,\tau)$ was approaching a constant. So we defined this value, $\lambda_{max}(\delta b,0)$, by:

$$\lambda_{max}(\delta b, 0) = \lim_{\tau \rightarrow 0} \lambda_{max}(\delta b, \tau) \qquad [4.4\text{-}6]$$

However, for very a small initial trajectory separation, a computational problem arose. The smaller the value of τ, the more iterations were needed to integrate the trajectories to infinity. This was a particular problem for potentials with large scattering regions. So we approximated this limit by plotting $\lambda_{max}(\delta b,\tau)$ as a function of τ (Figure 4.3) and finding the intercept (where τ=0). We took the 40 smallest values of the time step to generate $\lambda_{max}(\delta b,0)$.

Now that we had eliminated the dependence of the Lyapunov exponent upon the time step, we needed to eliminate it in the initial separation as well. If the values chosen for δb were too large, then the two trajectories could be on entirely different fixed points. This could lead to overly large values for the Lyapunov exponent. However, too small a δb and the two trajectories could stay too close together in time (leading to lower values of λ than was accurate). We then averaged twenty values of $\lambda_{max}(\delta b_i,0)$ with δb in the range of $.005 \geq \delta b_i \geq .001$. We compared our results to published data (9) and discovered that our method was valid to at least two significant figures.

Using the methods presented in this chapter we were able to calculate geometric and dynamic properties of all ten potentials.

5. DATA AND RESULTS

We could have presented the 600 scattering functions that our experiment produced. Instead, we presented representatives of the raw data. This will included: the difference between chaotic and nonchaotic data, how the delay time and scattering angle are equivalent for analysis, how the scattering functions are fractal, and how the scattering functions change with energy. We will then concentrated on a single chaotic energy of each potential and compared the resultant scattering functions. Next, we gave the results of our Lyapunov exponent and capacity dimension experiments. Finally, we presented the critical energy results using two different methods. By each figure we have placed a schematic of the investigated scattering system, for clarity.

5.1. SCATTERING FUNCTIONS

In this subsection we examined the way the scattering function changed as a function of energy for each of the potentials. These scattering function plots allowed us to define the scattering regions presented in the previous section. We began with a well behaved example, V_{2A}.

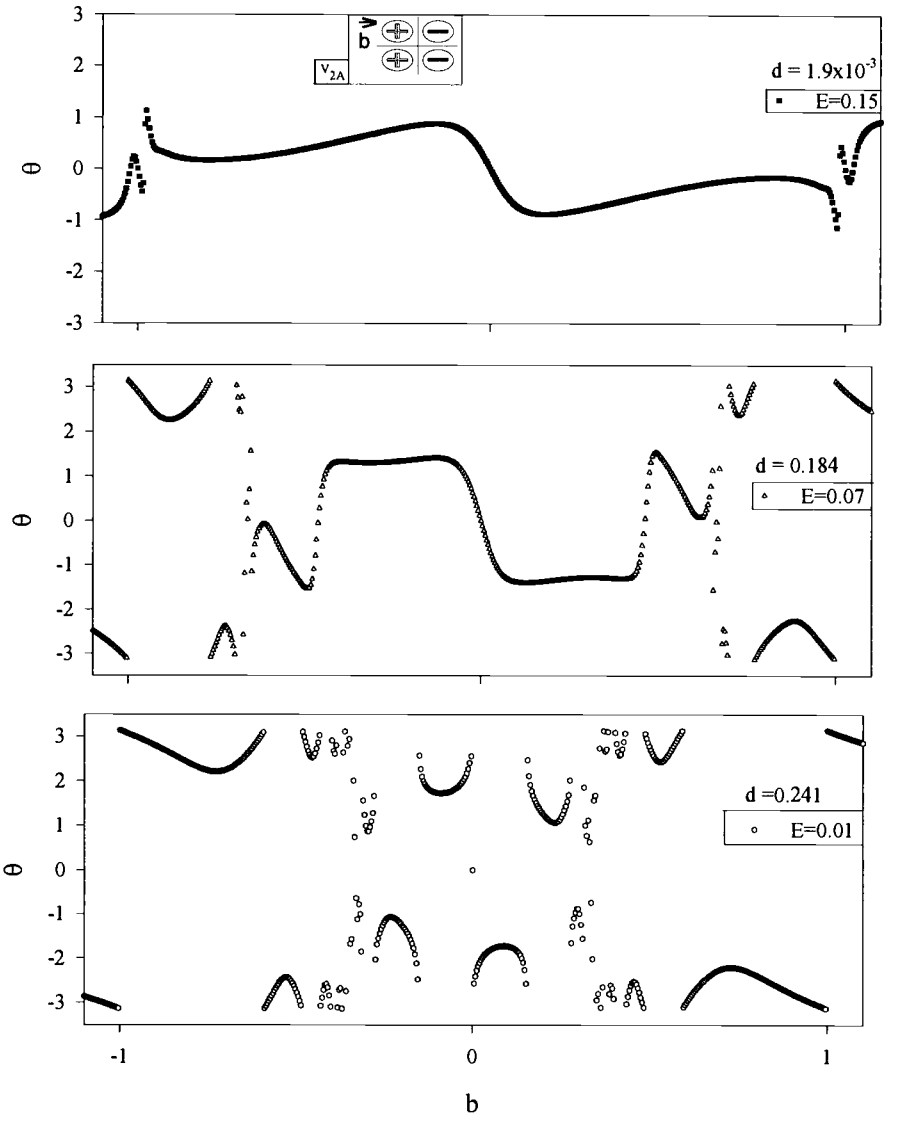

Figure 5.1 – Scattering angle, θ, as a function of impact parameter, b, for V_{2A} at: (top) E=0.15, (middle) E=0.07, and (bottom) E=0.01. All three have the same scale for the b-axis. The capacity dimension, d, is also shown. The potential schematic show in the top figure is the same for each of them.

It was apparent as the energy decreases, the figures became more chaotic, and the capacity dimension increased. While the lower energy figures seemed to have regions of noise, we knew that this is not the case. Each of the energies had a

well-defined capacity dimension, and thus a regular geometric structure of some kind. From the capacity dimension for the top figure, we concluded that at E=0.15, there are no trapped periodic orbits. The discontinuities at $b = \pm 1$ corresponded to the particle striking one of the centers directly. The relationship between energy and capacity dimension will be examined further in Section 5.3.

Fractal structure was visually verified by using the plot at the bottom of Figure 5.1. We took this figure and performed successive magnifications on it. This was shown in Figure 5.2.

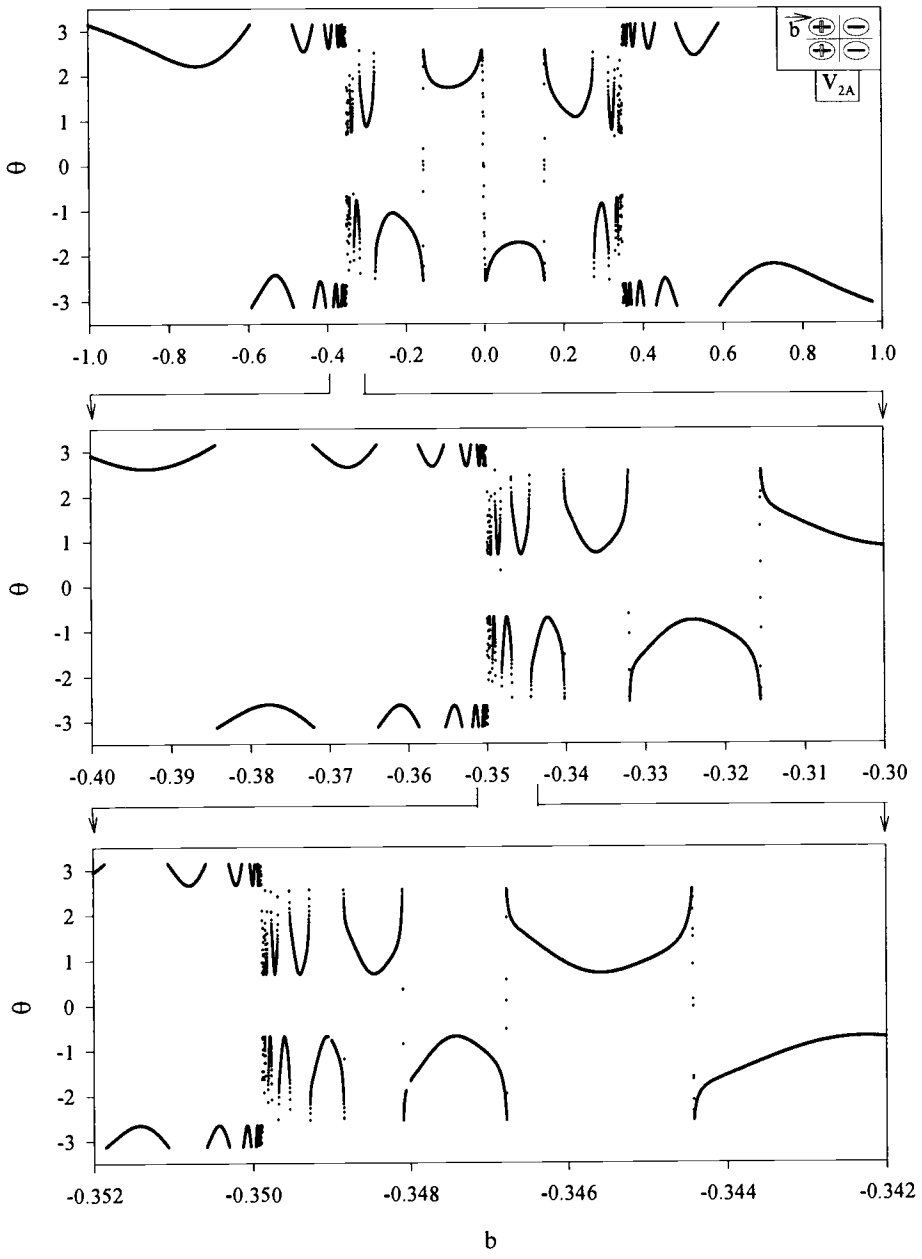

Figure 5.2 – Visually verifying the fractal nature of the scattering function (scattering angle, θ, vs. impact parameter, b,) for V_{2A} at E=0.01, by successive magnification.

It was apparent that each successive region contained areas of regularity and discontinuity. The "almost" self-similarity shown in Figure 5.2 made us conclude the structure was indeed a fractal. In the language of chaotic scattering these discontinuities were referred to as "singularities". The particle became nearly trapped at these points, and approached an infinity period. But the term is really just a bit of poetic license used in this field.

Next we examine how the scattering angle tends to change with increasing energy. Figure 5.3 shows an overview of the trend associated with V_{2A}.

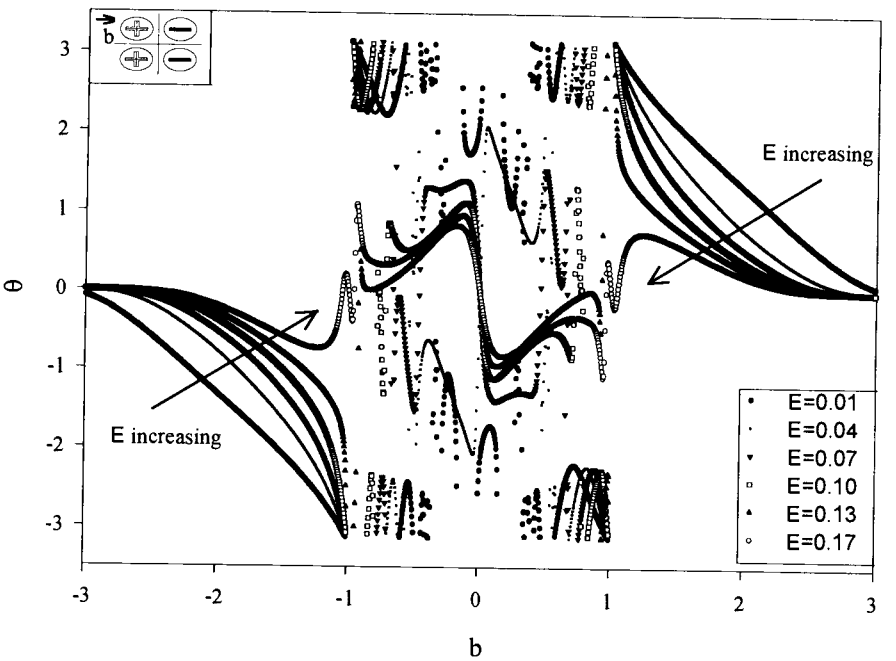

Figure 5.3 – Scattering angle, θ, as a function of impact parameter, b, for V_{2A} over a wide range of energies.

The above figure was very complicated and hard to understand , but we saw that the system became more regular with increased energy. In addition, there was a smaller range of possible θ values as the energy increases.

There were two different output parameters in our scattering experiment, scattering angle and delay time. For qualitative measurements of chaos, they were both related. We show this in Figure 5.4, below:

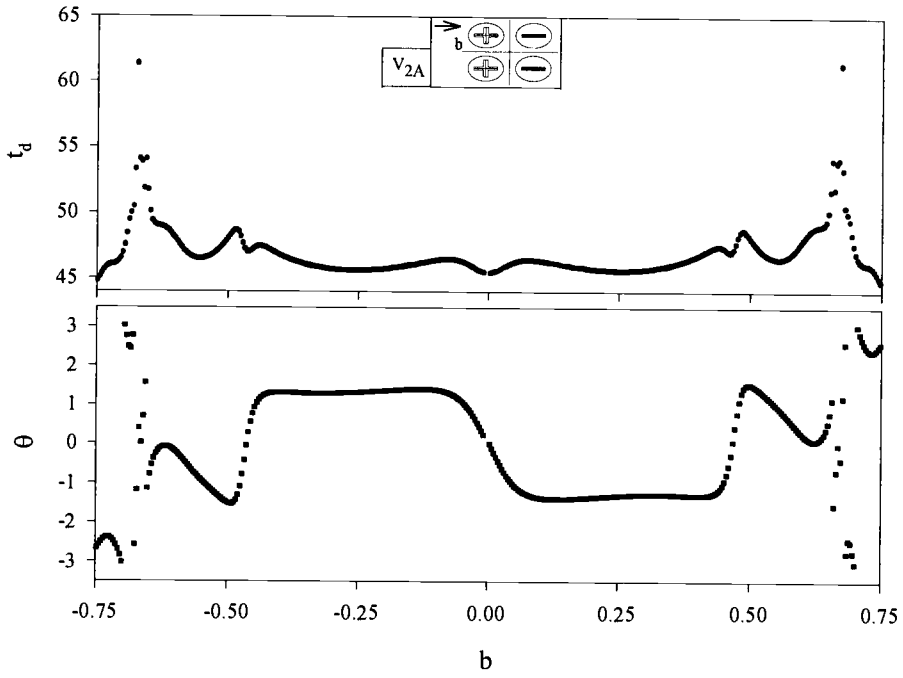

Figure 5.4 – Scattering functions for V_{2A} at E=0.07 using (top) delay time, t_d, (bottom) scattering angle, θ, as a function of the impact parameter, b. The b-axis scale is the same for both plots.

It was apparent that both the t_d and the θ plots had singularities in the exact same places. So, for chaos measurements, either output function would suffice. In Section 4 we showed that chaos in a scattering system arose when a particles started out close to the stable manifold and almost became trapped by the system. When this happened, the delay time would be significantly larger than a nearby particle that did not come close to being trapped. The delay time gave a tangible indication

of where particles were becoming trapped. For this reason, we used the delay time in our scattering functions.

At lower energies, the delay time was larger for two reasons. Since higher energy particles traveled faster, they spent less time inside the scattering region. Also, a lower energy particle would be more susceptible to the influence of the potential, and gave it a greater chance to become trapped. All of the potentials showed this behavior.

Now we began to analyze the time delay functions. We started with the most discontinuous, V_1.

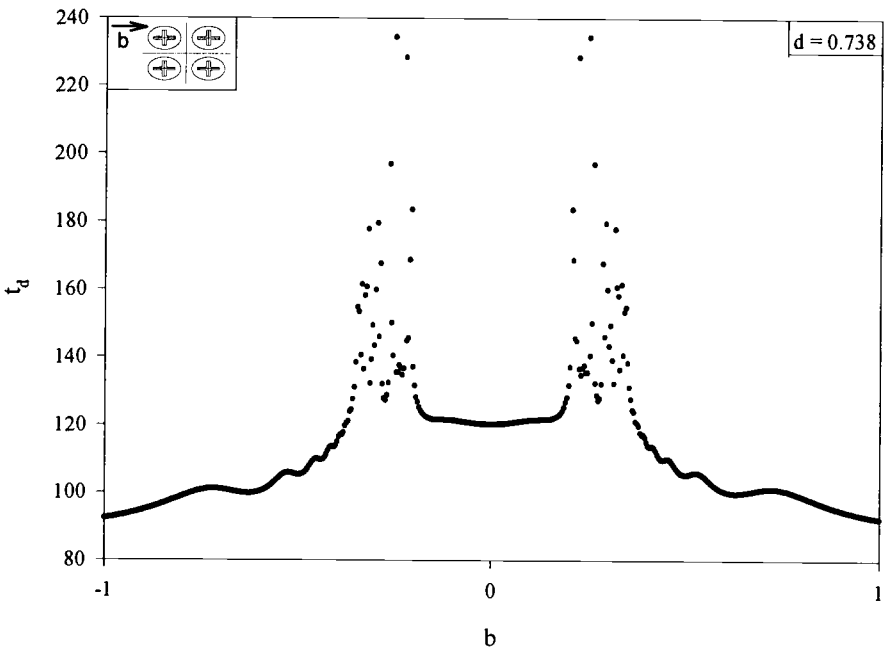

Figure 5.5 – Delay time, t_d, as a function of impact parameter, b, for V_1 at E=0.01.

At first glance, Figure 5.5 seemed to depict pure random noise. However, careful examination revealed that it was perfectly symmetric about the b=0 line. In

addition it had a well-defined capacity dimension (that was very high). This indicated an underlying complicated geometry.

We showed in Figure 5.3 how the scattering angle changed with energy. This was a complicated figure and difficult to understand. We present a similar plot using the delay time:

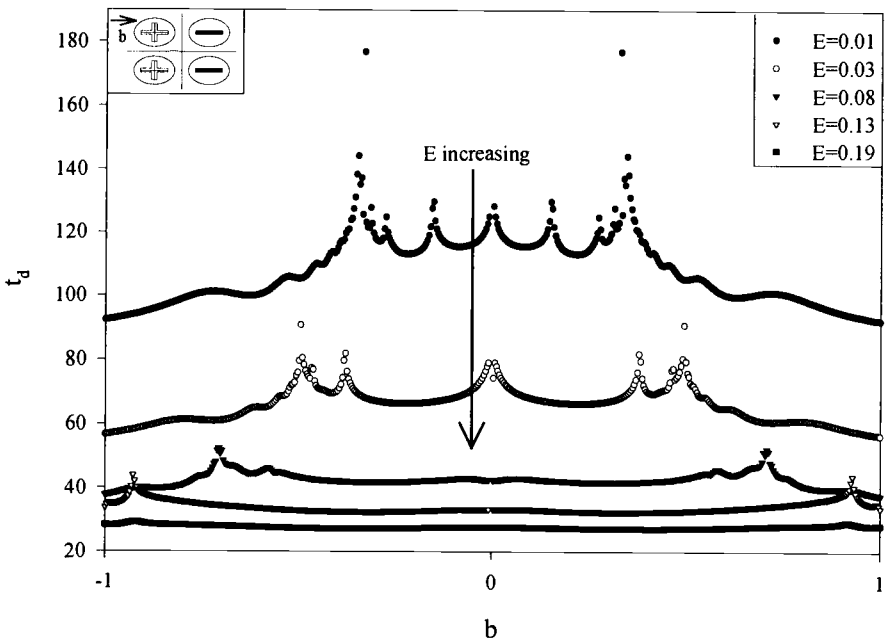

Figure 5.6 – Delay time, t_d, as a function of impact parameter, b, for V_{2A} at many energies. The arrow indicates direction of increasing energy.

We found it easier to see trends in the above figure than that of Figure 5.3. As expected, the delay time decreases with increasing energy. At energies below some critical value, there were discontinuities.

We found it interesting to compare the delay times for the different potentials at a low (chaotic) energy. We defined the "front face" to be the sign of

the first two potential hills that the particle feels. Since the particle was incident from the left, these are the signs of the hills in Quadrants II and III. For reasons that will become apparent, we divided our potentials into three groups based upon this front face. We started with the all positive front face given by potentials V_1, V_{5B}, and V_{2A}.

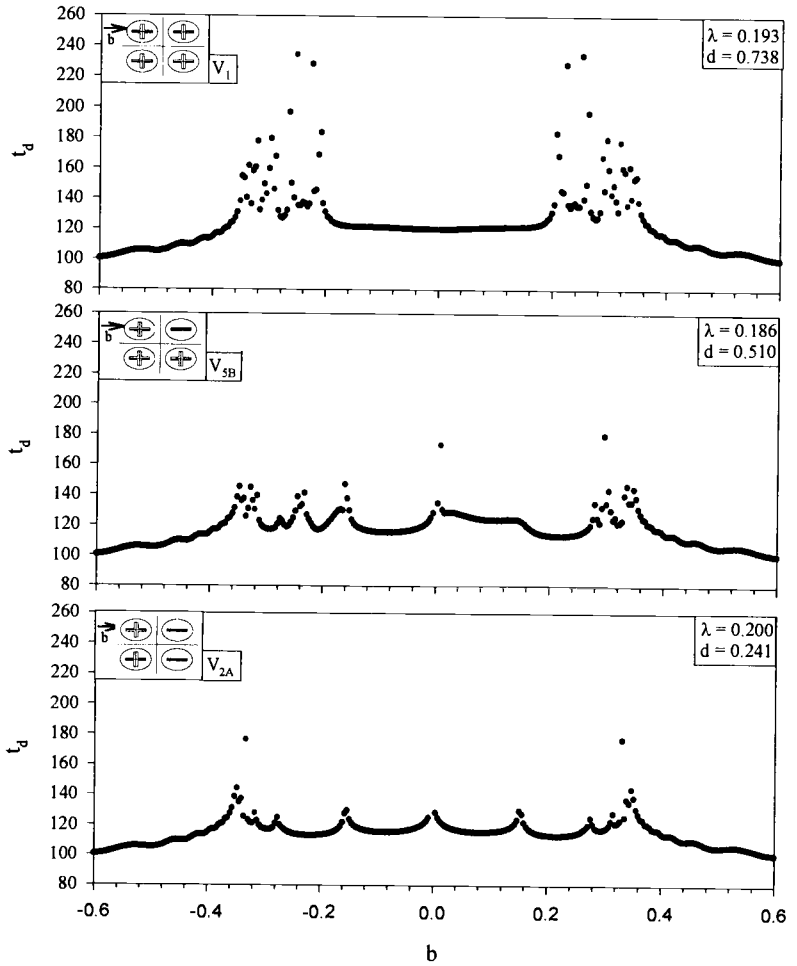

Figure 5.7 – Delay time, t_d, as a function of impact parameter, b, for potentials with an all positive front face: (top) V_1, (middle) V_{5B}, and (bottom) V_{2A} at E=0.01. These all have the same b and t_d axes.

These three systems have two positive wells in front. Figure 5.7 showed the progression of the system from two positive wells behind to two negative wells behind. As we added the attractive potentials, the delay time decreased. Also note that the fractal dimension decreased as well. This was apparent visually as the top system had more singularities than the bottom system. However, the Lyapunov exponent of these three systems was almost equal. We presented the Lyapunov exponents in Section 5.2, capacity dimension in Section 5.3, and discussed how they quantify chaos differently in our conclusions, Section 6.

Now we turned our attention to the cases where the front face had two negative wells. These were the potentials V_{2B}, V_{4B}, and V_6.

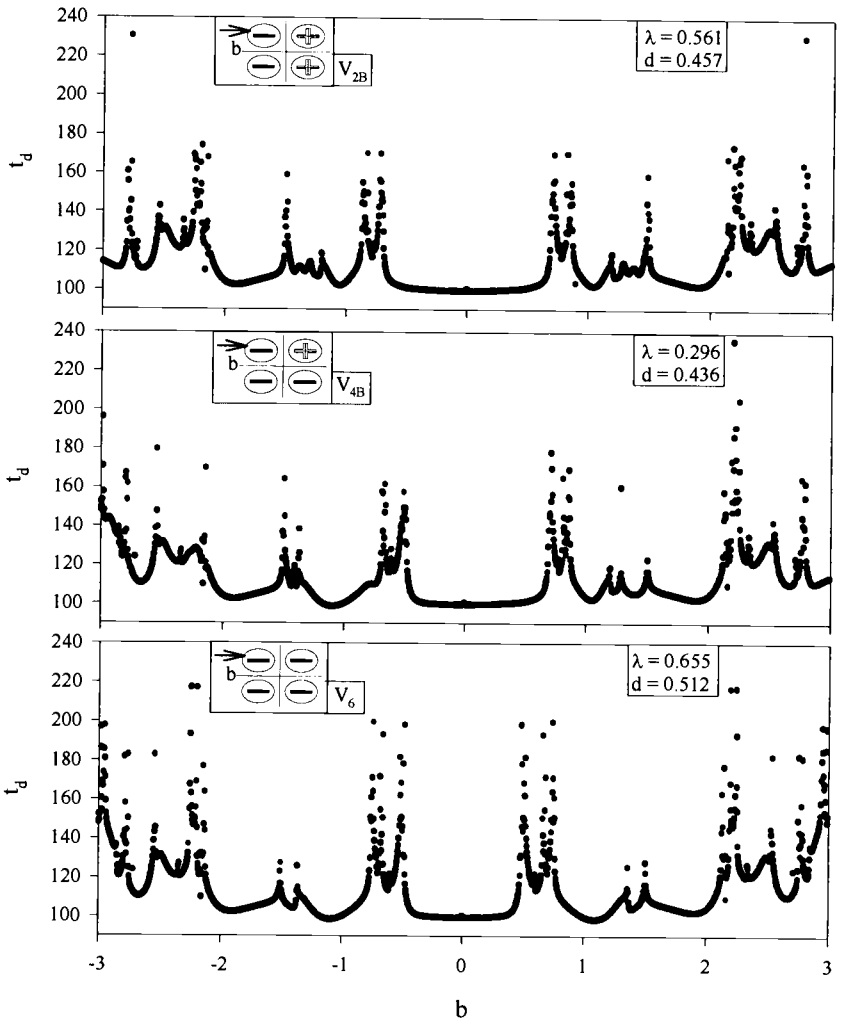

Figure 5.8 – Delay time, t_d, as a function of impact parameter, b, for potentials with an all-negative front face: (top) V_{2B}, (middle) V_{4B}, and (bottom) V_6 at E=0.01. These all have the same b and t_d axes.

Note that while all of the plots in Figure 5.8 had the same pattern, they were completely different than that of Figure 5.7. Finally, we presented the scattering function of the potentials with a positive and a negative front face (what we called a "split face"), V_{5A}, V_3, V_{2C}, and V_{4A}, in Figure 5.9.

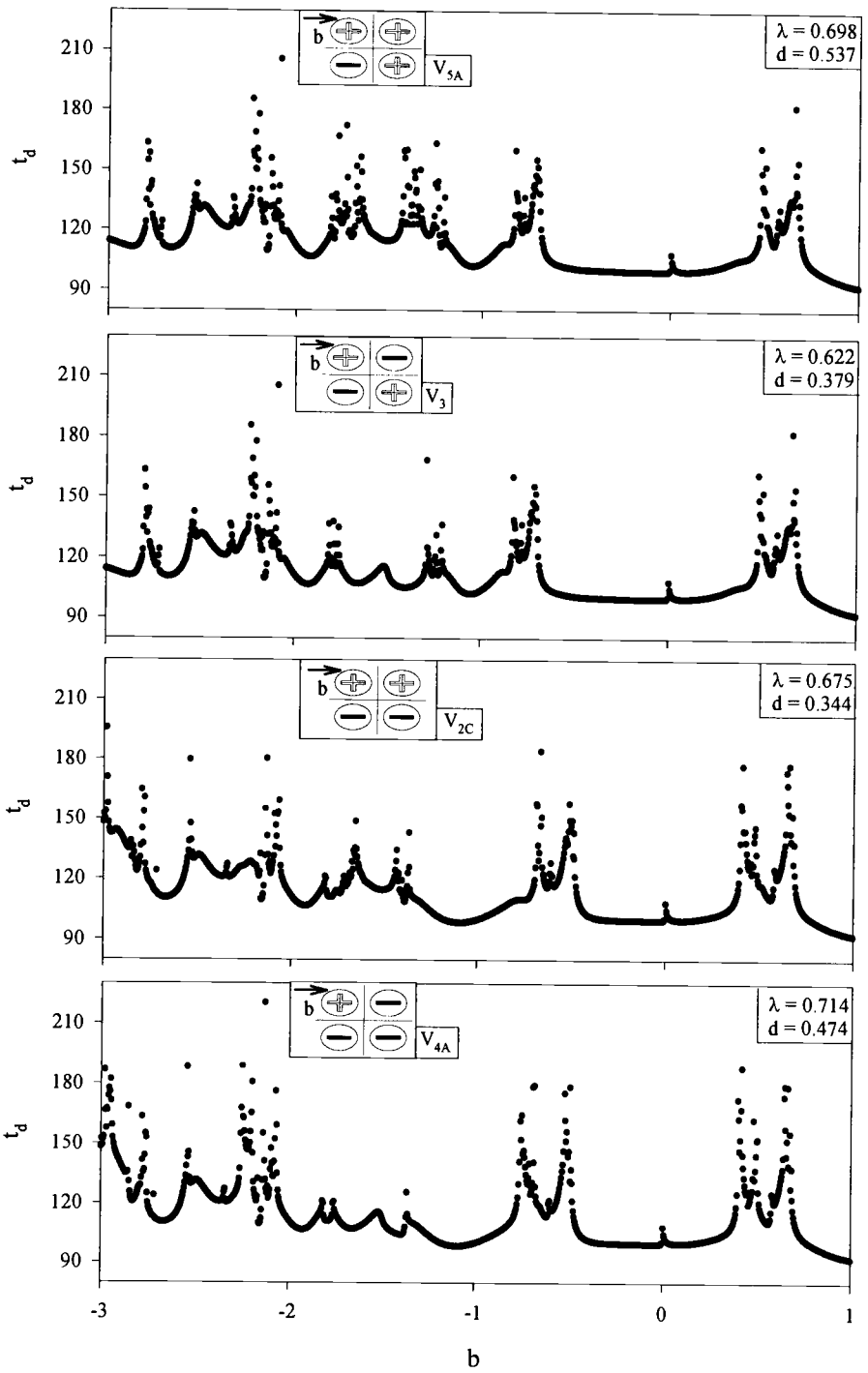

Figure 5.9 – Delay time, t_d, as a function of impact parameter, b, for potentials with a split front face: (top) V_{5A}, (upper middle) V_3, (lower middle) V_{2C}, and (bottom) V_{4A} at E=0.01. These all have the same b and t_d axes.

Again we saw that the potentials that had the same front face had similar scattering functions. In the next two subsections, we investigated if this pattern carried over to the measurement of chaos.

5.2. LYAPUNOV EXPONENT

We now investigated our Lyapunov exponent results for the ten different potentials. We plotted the Lyapunov exponent as a function of energy and made fits of the data. These figured showed two distinct regions. Below some energy, the behavior was be governed by one type of equation (discussed shortly). However, above some energy, the system had a linear response. We made fits of both halves of the figure, tabulated regression statistics and equations, and indicated the intersection of these two fits on the graphs.

5.2.1. Lyapunov exponent as a function of energy

We began with the potentials with an all positive front face. The regression results for the fits shown in Figures 5.10 to 5.12 are found in Section 5.2.2.

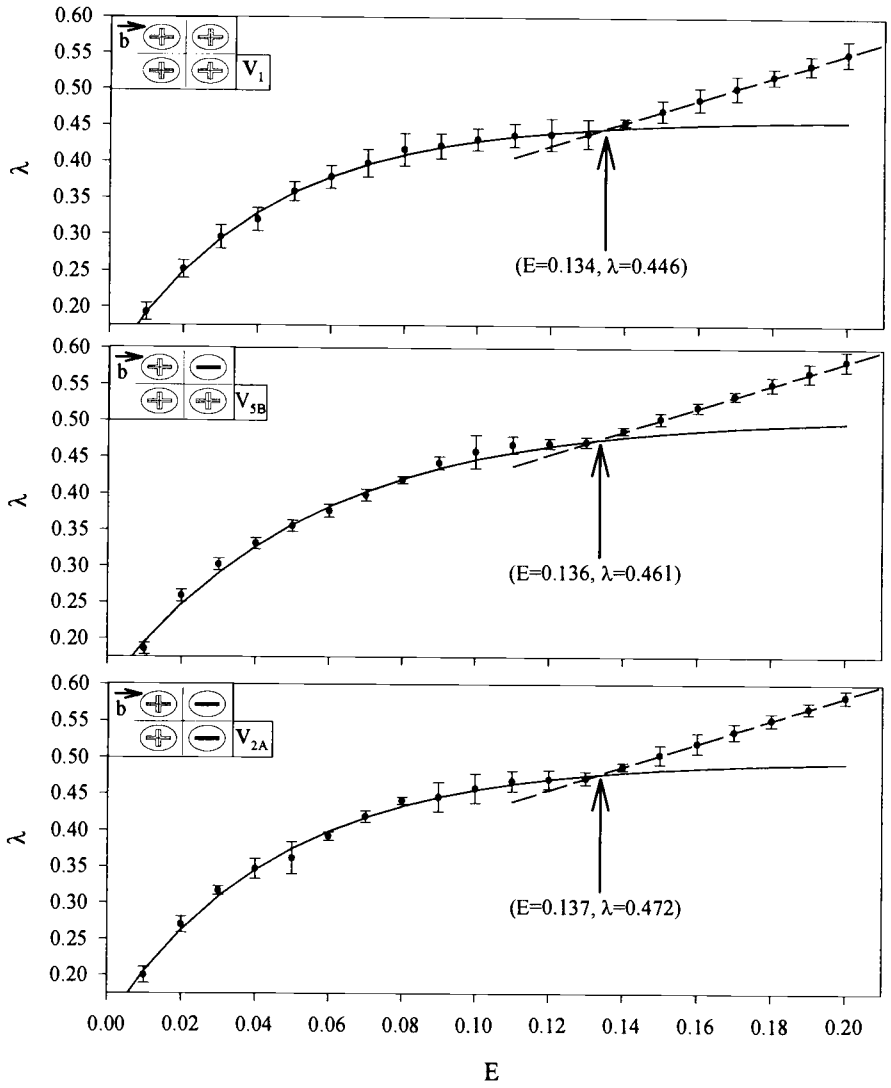

Figure 5.10 – Lyapunov exponent, λ, as a function of energy, E, for potentials with an all positive front face: (top) V_1, (middle) V_{5B}, and (bottom) V_{2A}. Statistics for the regression lines are given in Table 5.1.

All three potentials had very similar Lyapunov shapes. It was very apparent that there were two separate behaviors in this system.

We now looked at the potentials that had an all-negative front face.

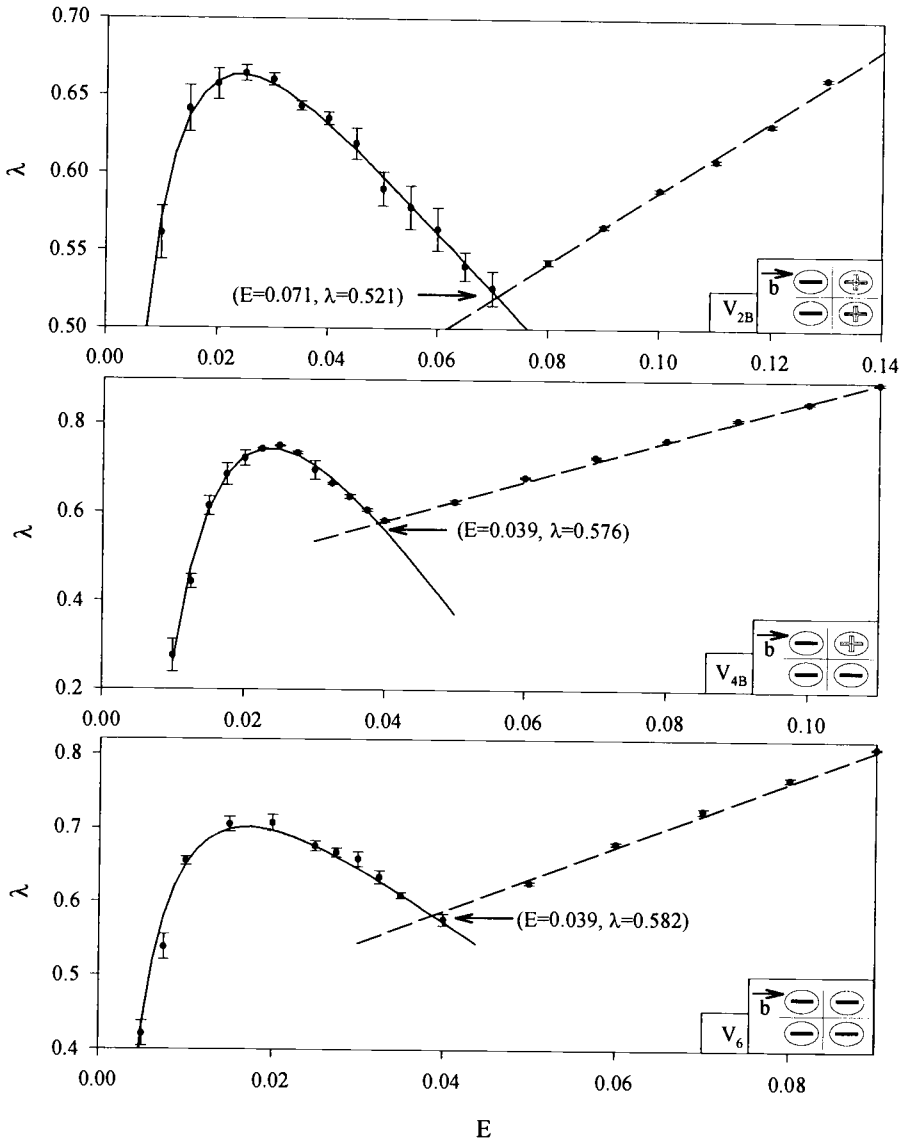

Figure 5.11 – Lyapunov exponent, λ, as a function of energy, E, for potentials with an all negative front face: (top) V_{2B}, (middle) V_{4B}, and (bottom) V_6. Statistics for the regression lines are given in Table 5.2.

It was important to notice that these three all had a very similar shape. While the potentials had reasonable fits, they did not have the same form as those in Figure 5.10. Finally we analyzed the potentials with a split front face.

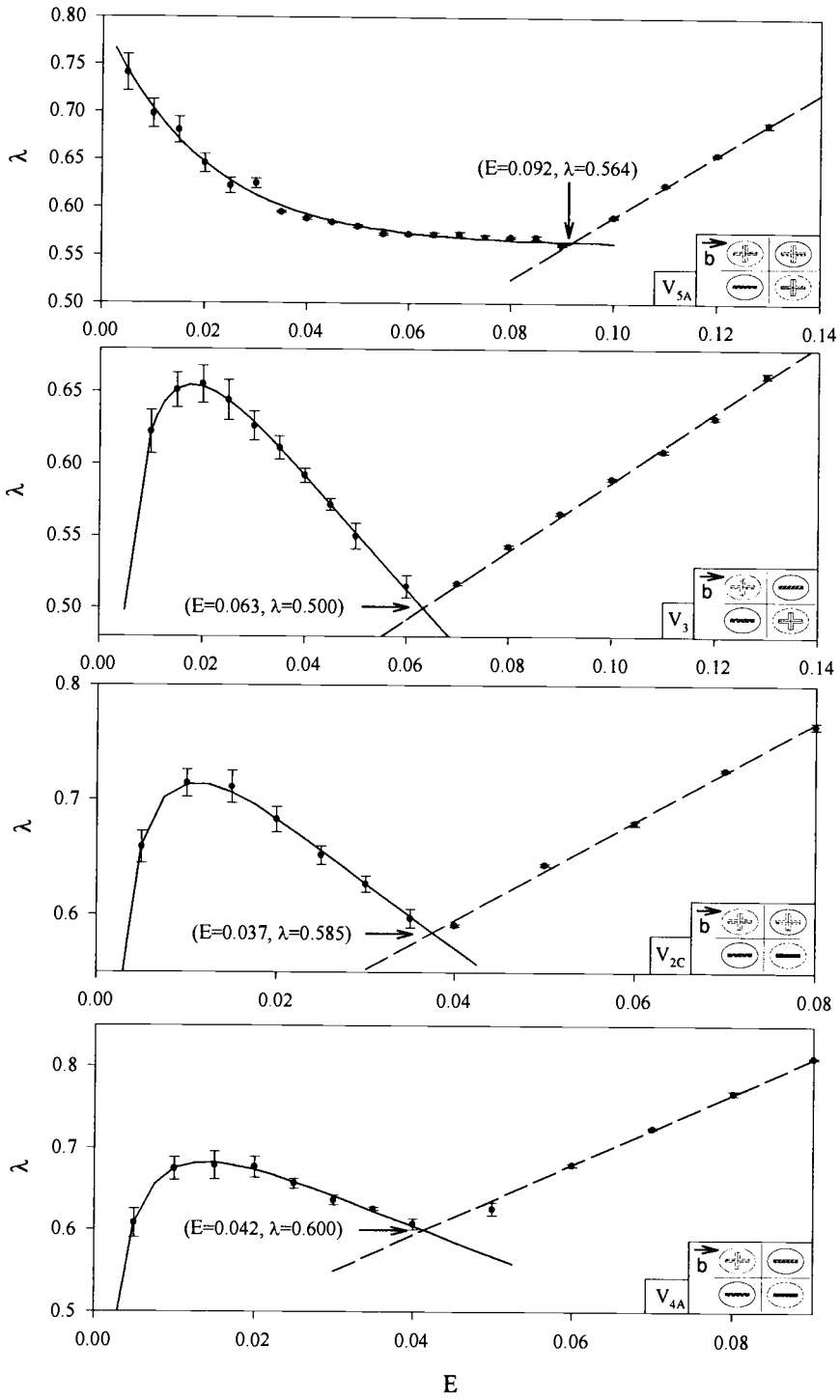

Figure 5.12 – Lyapunov exponent, λ, as a function of energy, E, for potentials with a split front face: (top) V_{5A}, (upper middle) V_3, (lower middle) V_{2C}, and (bottom) V_{4A}. Statistics for the regression lines are given in Tables 5.3a and 5.3b.

While three of the potentials had a similar shape to those in Figure 5.11, V_{5A} had a very different behavior. Because of this, we gave this potential's regression statistics separately.

5.2.2. Regression results for the Lyapunov exponents

The regression results of the fit lines shown in Figures 5.10 to 5.12 where entered into the following tables. Table 5.1 was for the potentials with an all positive front face. Table 5.2 was for potentials with an all negative front face. Tables 5.3a and 5.3b were for the potentials with a split front face.

Table 5.1 – Regression results for Lyapunov data (Figure 5.10) of potentials with all positive front face: V_1, V_{5B}, and V_{2A}.

	left: $\lambda=\lambda_0 + a(1 - e^{-bE})$				right: $\lambda= mE + b_i$		
Potential	λ_0	a	b	R^2%	m	b_i	R^2%
V_1	0.119 ± 0.007	0.340 ± 0.006	24.2 ± 1.2	99.7	1.60 ± 0.01	0.231 ± 0.002	99.8
V_{5B}	0.133 ± 0.011	0.374 ± 0.009	18.3 ± 1.7	99.4	1.61 ± 0.01	0.262 ± 0.002	99.6
V_{2A}	0.135 ± 0.011	0.362 ± 0.008	21.8 ± 1.6	99.4	1.60 ± 0.01	0.264 ± 0.002	99.5

Table 5.2 – Regression results for Lyapunov data (Figure 5.11) of potentials with all negative front face: V_{2B}, V_{4B}, and V_6.

	left: $\lambda=\lambda_0 + a\ln(E) + b\ln^2(E)$				right: $\lambda= mE + b_i$		
Potential	λ_0	a	b	R^2%	m	b_i	R^2%
V_{2B}	-1.02 ± 0.06	-0.899 ± 0.004	-0.120 ± 0.005	98.7	0.357 ± 0.001	2.32 ± 0.002	99.9
V_{4B}	-8.47 ± 0.09	-4.92 ± 0.01	-0.656 ± 0.003	97.9	0.399 ± 0.001	4.53 ± 0.002	99.6
V_6	-2.24 ± 0.08	-1.78 ± 0.01	-0.178 ± 0.002	98.1	0.412 ± 0.002	4.40 ± 0.002	99.7

Table 5.3a – Regression results for Lyapunov data (Figure 5.12) of three potentials with a split front face: V_3, V_{2C}, and V_{4A}.

	left: $\lambda=\lambda_0 + a\ln(E) + b\ln^2(E)$				right: $\lambda = mE + b_i$		
Potential	λ_0	a	b	R^2%	m	b_i	R^2%
V_3	-0.914 ± 0.033	-0.779 ± 0.019	0.096 ± 0.002	98.5	0.349 ± 0.003	2.39 ± 0.04	99.8
V_{2c}	-0.600 ± 0.022	-0.601 ± 0.016	0.116 ± 0.007	97.8	0.420 ± 0.004	4.34 ± 0.04	99.7
V_{4A}	-1.041± 0.001	-0.779 ± 0.002	-0.086 ± 0.001	99.4	0.424 ± 0.004	4.30 ± 0.03	99.9

Table 5.3b – Regression results for Lyapunov data of V_{5A} (Figure 5.12).

	left: $\lambda=\lambda_0 + a\,e^{-bE}$				right: $\lambda = mE + b_i$		
Potential	λ_0	a	b	R^2%	m	b_i	R^2%
V_{5A}	0.562 ± 0.003	0.233 ± 0.008	50.2 ± 3.4	97.9	0.265 ± 0.004	3.26 ± 0.002	99.1

5.2.3. Calculating λ_{max}

To compare the dynamic chaos of each of the system, we found the largest Lyapunov exponent over the whole energy range shown in Figures 5.8 to 5.9. For those that had a power log type fit, we calculated the maximum Lyapunov exponent by taking the derivative of the fit function (to find the energy where the derivative was zero, E_{peak}). For the others (V_1, V_{5B}, V_{2A}, V_{5A}), we used the maximum value from the data set. By averaging the uncertainties of the Lyapunov exponents in the region of E_{peak}, we arrived at an estimate of the uncertainty in the λ_{max}.

Table 5.4 – Maximum Lyapunov exponent, λ_{max}, for each potential. The list was organized in descending order. The face type was given by P = all positive, N = all negative, and S = split face.

Potential	λ_{max}	Face Type
V_1	0.446 ± 0.013	P
V_{5B}	0.461 ± 0.006	P
V_{2A}	0.472 ± 0.007	P
V_3	0.655 ± 0.011	S
V_{2B}	0.663 ± 0.007	N
V_{2C}	0.683 ± 0.010	S
V_6	0.697 ± 0.008	N
V_{4A}	0.714 ± 0.010	S
V_{5A}	0.741 ± 0.009	S
V_{4B}	0.743 ± 0.003	N

The data in Table 5.4 was plotted in Figure 5.13 for easier comparison of the maximum Lyapunov exponent.

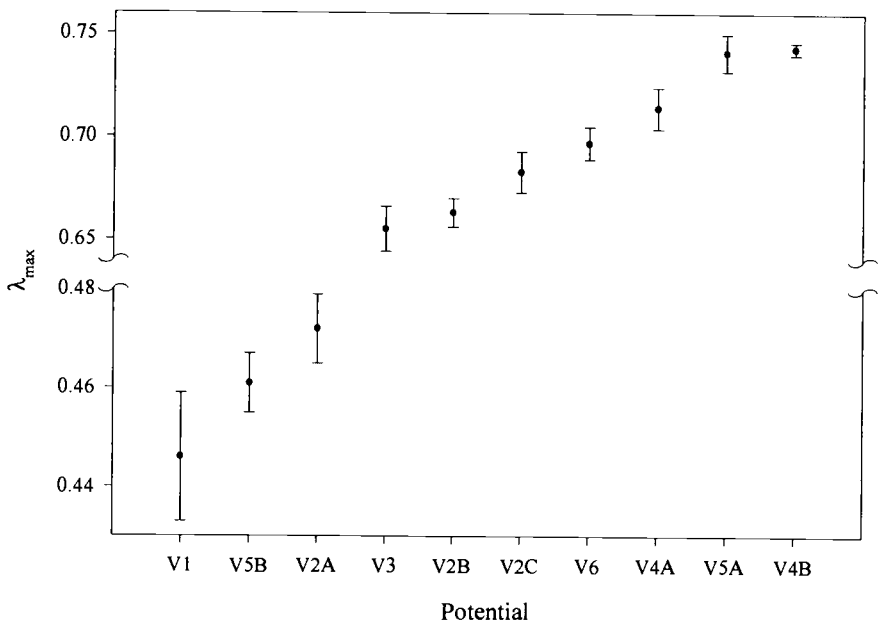

Figure 5.13 - λ_{max} for each of the ten potentials. The break in the λ_{max}-axis indicates that the number range from 0.48 to 0.64 has been removed.

We will return to this figure in Section 6 when we discuss how chaotic the different systems are.

5.3. CAPACITY DIMENSION

Using the uncertainty exponent technique, we found the capacity dimension, d, as a function of energy for each of the potentials. As before, we split these into groups based upon their front face.

We started with V_1, V_{5B}, and V_{2A}. These are all shown in Figure 5.14.

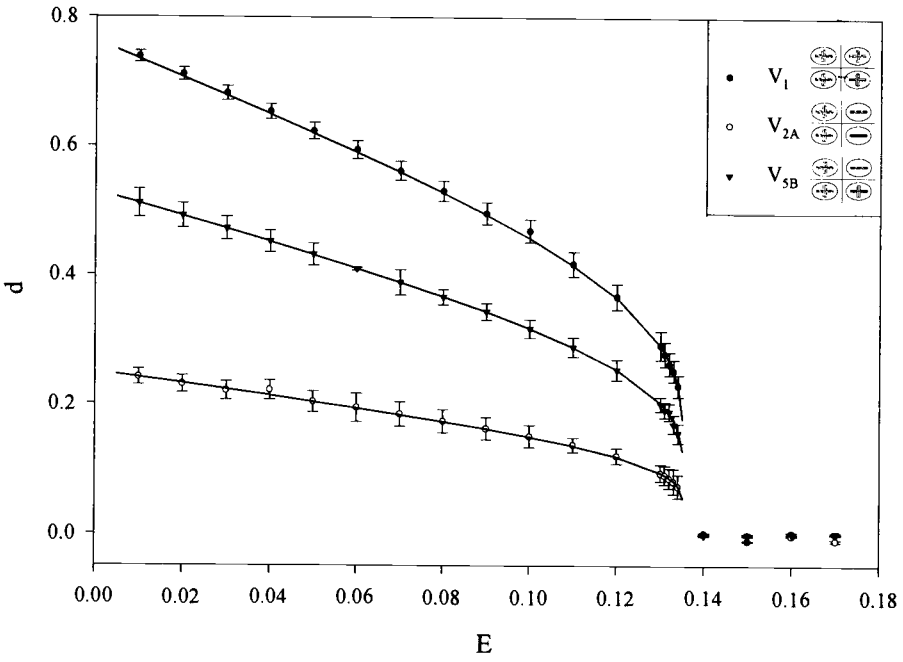

Figure 5.14 – Capacity dimension, d, as a function of energy, E, for potentials with an all positive front face: V_1, V_{5B}, and V_{2A}. The regression lines are given by $d=m\ \ln^{-1}(E_c-E)^{-1}$, Equation 3.2-5. Where E_c is the critical energy and m is the proportionality constant. The regression results are shown in Table 5.5.

We noticed that the capacity dimension decreased rapidly to zero. This was characteristic of capacity dimension behavior near the critical energy. This energy could simply be measured from the regression results of Table 5.5.

Table 5.5 – Regression results of using Equation 3.2-5 on the capacity dimension results of Figure 5.14.

	$d=m\ \ln^{-1}(E_c-E)^{-1}$		
Potential	E_c	m	R^2%
V_1	0.135 ± 0.002	1.523 ± 0.013	99.4
V_{5B}	0.135 ± 0.002	0.501 ± 0.001	99.8
V_{2A}	0.135 ± 0.002	1.060 ± 0.010	99.3

Below are the capacity dimension results for the potentials with an all negative front face:

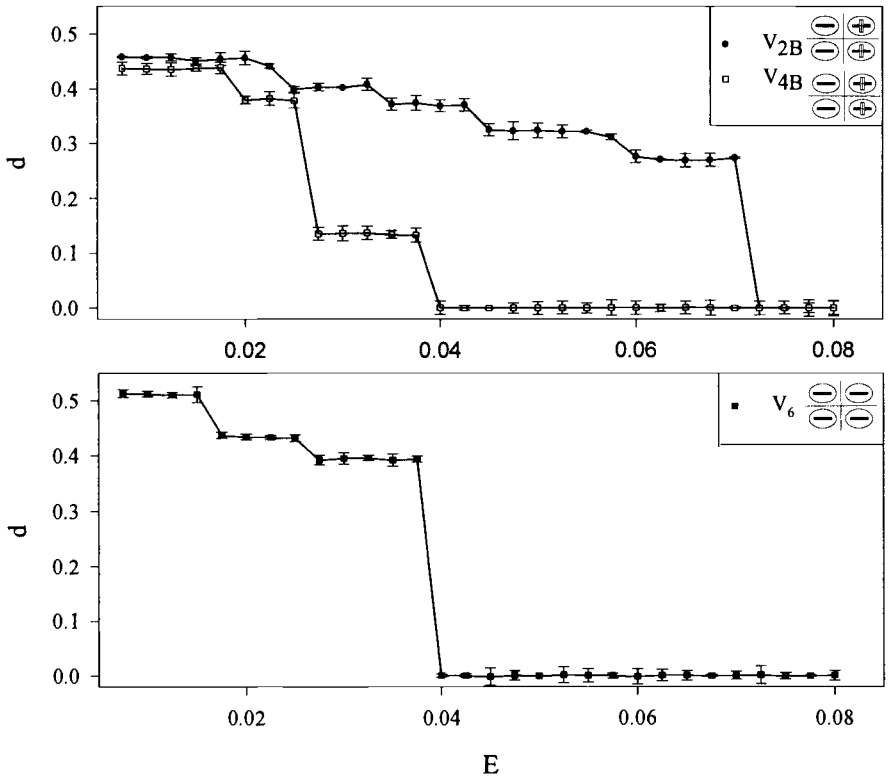

Figure 5.15 – Capacity dimension, d, as a function of energy, for potentials with an all negative front face: (top) V_{2B}, V_{4B}, and (bottom) V_6.

This pattern of constant plateaus is the "devil's staircase" that was referred to in Section 3.2.2. Finally we finished up with the potentials with a split front face: V_{5A}, V_{4A}, V_3, and V_{2C}.

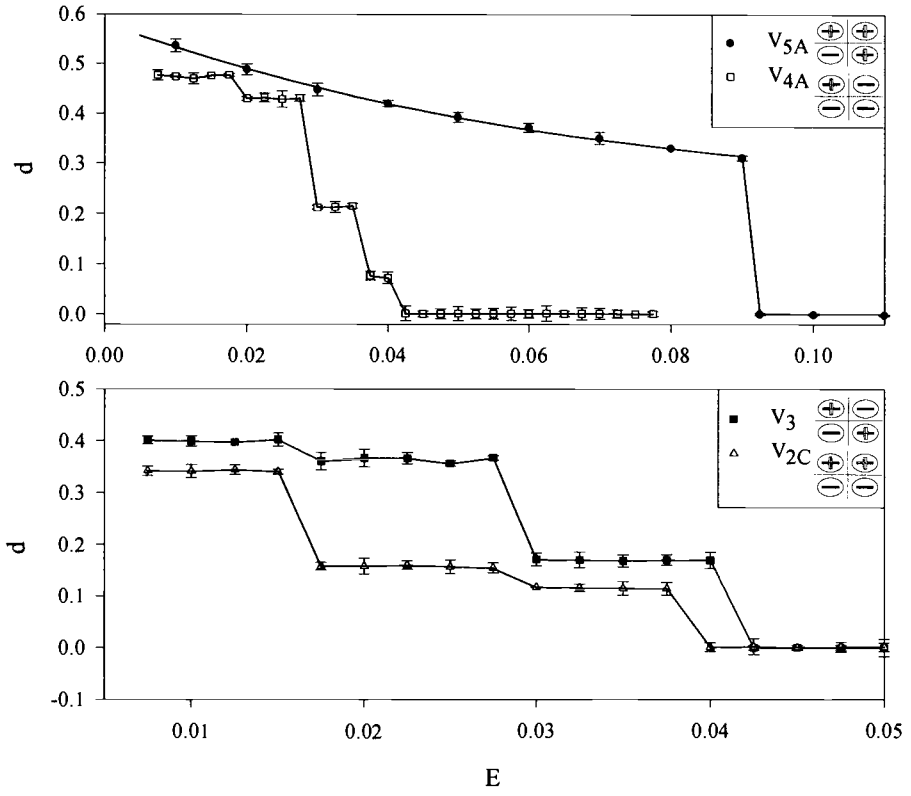

Figure 5.16 – Capacity dimension, d, as a function of energy, for potentials with a split front face: (top) V_{5A}, V_{4A}, (bottom) V_3, and V_{2C}.

All of the potentials in Figure 5.16 had a devil's staircase with the exception of V_{5A}. We fitted this with a standard exponential decay and the results of this fit are shown in Table 5.6.

Table 5.6 – Regression results for capacity dimension, d, data for the V_{5A} potential.

	$d=d_0 + a\, e^{-bE}$			
Potential	d_0	a	b	R^2%
V_{5A}	0.220 ± 0.013	0.364 ± 0.001	15.0 ± 1.5	99.5

5.4. CRITICAL ENERGY

Above some critical energy, the system had no periodic orbits. This critical energy was measured two different ways. In the first, we simply observed where the capacity dimension went to zero in Figures 5.14 to 5.16. The second way took advantage of the fact that when the system bifurcated, the Lyapunov exponent would change its behavior. We simply equated the fits from the left and right side, of Figures 5.10 to 5.12, to each other.

Table 5.7 – E_c using the Lyapunov exponent, λ, data and the capacity dimension, d, data. % Deviation is given by: $\left|E_c(\lambda) - E_c(d)\right| \Big/ \sqrt{\Delta E_c(\lambda)_1^2 + \Delta E_c(d)^2}$.

	λ - data	d - data	% Deviation
V_1	0.135 ± 0.002	0.135 ± 0.002	0.0%
V_{2A}	0.137 ± 0.002	0.135 ± 0.002	70.7%
V_{2B}	0.071 ± 0.002	0.071 ± 0.001	0.0%
V_{2C}	0.037 ± 0.002	0.038 ± 0.002	35.4%
V_3	0.037 ± 0.002	0.040 ± 0.002	106.1%
V_{4A}	0.042 ± 0.002	0.041 ± 0.001	44.7%
V_{4B}	0.039 ± 0.003	0.038 ± 0.002	27.7%
V_{5A}	0.092 ± 0.003	0.091 ± 0.002	27.7%
V_{5B}	0.136 ± 0.002	0.135 ± 0.002	35.4%
V_6	0.039 ± 0.002	0.039 ± 0.001	0.0%

%Deviation was a measure of how closely the two values (and their errors) overlapped.

The previous table showed that the two methods were equivalent for finding the critical energy. V_3 had the highest %Deviation because the two values barely overlapped.

6. SUMMARY AND CONCLUSIONS

In this section, we give a summary of our experiment and interpret the data from the previous section. We finish with some possible direction for future research.

6.1. EXPERIMENTAL SUMMARY

We investigated classical chaotic scattering in this experiment. In our scattering system, there were two main types of chaos. The first occurred when trajectories started out close to the stable manifold and almost became trapped in the chaotic set. Above a certain energy, the critical energy, there were no trajectories that could become trapped. For these higher energies, chaos was caused by the particle striking the potential surface directly.

We used ten different potentials that were similar. The potentials had four hills centered at $x=\pm1$ and $y=\pm1$ (only one hill in a quadrant). Each of the hills were identical in size and shape, but had different signs. These potentials are shown in Figures 2.1 to 2.9 and Table 2.1.

Since the system was a Hamiltonian one (conservative in energy), Hamilton's method (Section 2.1) was used to find the equations of motion. These were then reduced to a system of four 1^{st} order ordinary differential equations of motion (Equations 4.2-2a to 4.2-2d). We then used a 4^{th} order Runge-Kutta method to numerically integrate these equations.

The incident beam came from the left side from infinity. The distance above the x-axis was defined as the impact parameter. The particle interacted with the potential for a limited amount of time, and then exited the system to infinity.

Measurements were made of the delay time (amount of time the particle takes to exit to infinity) and scattering angle (angle made between the unperturbed incident path and the exit path at infinity). These output parameters were plotted as a function of impact parameter (Section 5.1). In our scattering system, chaos was observed when the output parameters varied widely for small differences in impact parameter. This showed up as "speckles" in the plots (Figures 5.2, and 5.7 to 5.9).

We measured both the dynamical (Lyapunov exponent) and geometrical (capacity dimension) properties of each potential over a range of energies (Sections 5.2 and 5.3). We also measured the critical energy using these two properties (Table 5.7).

6.2. CONCLUSIONS

We set out to investigate the scattering properties of our potential as we change the signs of the hills. We wanted to discover which, if any, of them would be chaotic. In addition, we had hoped to be able to relate the geometry of the potentials to their characteristics.

6.2.1. Basic chaos in our system

We will start with the most obvious and concrete conclusions. The Lyapunov exponents indicate that each and every potential has a region where it is chaotic. This is not unexpected. Since we knew that V_1 was chaotic, it would be strange if a more complicated (but similar) system had not been.

We see from Figures 5.7 to 5.9 that a similar front face gives a similar scattering shape. From this, we had hoped to be able to use simple geometry to

characterize the systems. This is true for the three potentials with two positive hills in front, V_1, V_{5B}, V_{2A}. These three potentials have almost exactly the same Lyapunov, critical energy, and capacity dimension results. They were are also very different than the other seven potentials. Unfortunately, when we examined the other potentials, the simple geometry broke down. There were not enough similarities to establish trends.

We believe that the three were so similar because of their front face. Once the particle had enough energy to penetrate the two positive hills, it would simply exit the system. The negative hills in Quadrant I and/or Quadrant IV, would have limited effect because they were not attractive enough.

There was some question as to which systems would be more chaotic. No studies have been done to compare the degree of chaos between systems with attractive and repulsive potentials. Our choice of potentials allowed for this kind of comparison to be made. It turned out that all of the potentials were more chaotic than the potential with four positive hills (V_1). So we reason that adding an attractive well to the potential makes it more chaotic than the all positive case. However, this does not mean that more attractors correspond to more chaos.

In fact, the two most chaotic potentials, V_{5A} and V_{4B}, do not even have the same number of negative wells. We were unable to find any connection between front face and chaos, besides the all positive front faces. Using the largest Lyapunov exponent, we were able to rank the potentials in degree of chaos: $V_{4B} = V_{5A} > V_{4A} > V_6 = V_{2C} > V_3 = V_{2B} >> V_{2A} > V_{5B} = V_1$. But did not see any geometry trends in this ranking.

We need to resolve the apparent disagreement between the capacity dimension and the Lyapunov exponent for measuring chaos. V_1 has the largest capacity dimensions, but it has the lowest Lyapunov exponent. However, it is not a simple inverse relationship because V_{2A} has the smallest capacity dimension and is just a little more chaotic than V_1. A larger capacity dimension means that the

chaotic set is larger (takes up more energy space), it doesn't dictate the dynamics of the system. While it does indicate that there will be more orbits that are almost trapped, it does not guarantee that they will be more chaotic. For this reason, we cannot compare the magnitude of capacity dimension to establish the degree of chaos.

6.2.2. Bifurcation and the critical energy

The capacity dimension data gives the best indication of the type of bifurcation (Section 3.2-2). We began with the potentials that had an all positive front face. From the literature about V_1 we knew that it was a generic abrupt bifurcation (3,9). We also had a scaling law for this specific type of bifurcation in our system (Equation 3.2-5). From the fits shown in Figure 5.2 and Table 5.5, we concluded that V_1, V_{5B}, and V_{2A} were all generic abrupt bifurcations.

Six of the remaining seven potentials had a capacity dimension that exhibited a devil's staircase pattern (see Figures 5.14 and 5.16). These patterns only occur in crisis type of bifurcations. These types of bifurcations were caused when two or more fixed points "collided" through a complex interaction of their stable and unstable manifolds. The steps were caused because of changes in chaotic set. The flat parts were when the chaotic set was constant and the abrupt jumps were when it changed to another constant. Since the staircase did not exist above a certain energy, this is an abrupt crisis bifurcation.

The potential that was not like any of the others was V_{5A}. It had a single negative hill in Quadrant III. For reasons that we could explain, it had entirely different characteristics than the others. Once the system reached the critical energy, the system suddenly jumped up to a value that was far from zero. This abrupt jump led us to believe that the chaotic set was already fully formed above the critical

energy, but access was prevented by KAM tori. These tori have been seen in only two types of bifurcations: abrupt nonhyperbolic and saddle-centre. We did not have the smooth increase from zero to unity that was characteristic of a saddle-centre bifurcation. So we were left, by process of elimination, to conclude that it was an abrupt nonhyperbolic bifurcation.

We turned our attention to the energy at which the bifurcation occurs, the critical energy. Geometry did play some role in the critical energy. The three potentials with an all positive front face had the same value for critical energy. If there was a negative hill in the front face, the critical energy would be lower. In comparing V_{5A} and V_{5B} (both have one negative and three positive hill), we saw that the one with the negative hill in front, V_{5A}, had a lower critical energy by about 47%. In looking at the transition from V_{2A} to V_{2B} to V_{2C}, we see that the critical energy dropped as we added more negative hills to the front face of the system.

Again, we could not use simple geometry to explain all of the characteristics of the critical energy. While V_{2C}, V_3, V_{4A}, V_{4B}, and V_6 are different in terms of geometry, they have very similar critical energies. So we were not able to use the critical energy as an indication of chaos.

In most of the literature, the critical energy was calculated by finding the energy for which the capacity dimension goes to zero. In our systems we also found that the behavior of the Lyapunov exponent could also be used. For energies below the critical energy, the Lyapunov energy scaled in one way and afterwards it scaled linearly. The intersection of these two lines occurred at the critical energy. The problem lies in finding an analytical fit for the Lyapunov exponent. In most cases it is generally a very complex relationship that does not have a simple equation. So while the method worked for this system, it is doubtful that it could be applied to a less symmetric type of system.

We also noticed that there was a connection between the fit equation for the Lyapunov exponent and that of the capacity dimension. In Table 6.1 we relate the fits for the characterizing data to the bifurcation type.

Table 6.1 – Bifurcation classification for the ten potentials and the fit equations used for Lyapunov exponent (λ) and capacity dimension (d).

	λ - fit	d - fit	Bifurcation
V_1	$\lambda_0 + a(1 - e^{-bE})$	$m \ln^{-1}(E_c\text{-}E)^{-1}$	generic abrupt
V_{2A}	$\lambda_0 + a(1 - e^{-bE})$	$m \ln^{-1}(E_c\text{-}E)^{-1}$	generic abrupt
V_{2B}	$\lambda_0 + a \ln(E) + b \ln^2(E)$	devil's staircase	abrupt crisis
V_{2C}	$\lambda_0 + a \ln(E) + b \ln^2(E)$	devil's staircase	abrupt crisis
V_3	$\lambda_0 + a \ln(E) + b \ln^2(E)$	devil's staircase	abrupt crisis
V_{4A}	$\lambda_0 + a \ln(E) + b \ln^2(E)$	devil's staircase	abrupt crisis
V_{4B}	$\lambda_0 + a \ln(E) + b \ln^2(E)$	devil's staircase	abrupt crisis
V_{5A}	$\lambda_0 + a e^{-bE}$	$d_0 + a e^{-bE}$	abrupt nonhyperbolic
V_{5B}	$\lambda_0 + a(1 - e^{-bE})$	$m \ln^{-1}(E_c\text{-}E)^{-1}$	generic abrupt
V_6	$\lambda_0 + a \ln(E) + b \ln^2(E)$	devil's staircase	abrupt crisis

From this we concluded that the bifurcation type had a profound impact on the behavior of the system both dynamically and geometrically.

6.2.3. Chaos above the critical energy

We will now try to make some sense of the linear response of the Lyapunov exponent at energies above the critical energy. We also hope to give some physical meaning to the regression statistics that have been generated in Section 5.2.2.

Once the system is above the critical energy, there is no possibility for trapping of a particle. The stable manifold simply does not intersect with the parameter space anymore. However, that does not mean that the stable and unstable

manifolds, or the chaotic set, has disappeared. We know from Equation 3.2-3 that the stable manifold (and thus the unstable one) has a dimension of two: a flat sheet. The chaotic set has a dimension of one (from Equation 3.2-4).

This is a very simple picture in energy space. We have two planes that intersect along a single line. For energies that are above the critical energy, but are not much larger (such as those we studied in this experiment), the system does not change behavior again. In other words, once the system is above the critical energy, the stable and unstable manifolds do not move.

We showed previously that the fixed points of these potentials are at the centers of each hill. Above the critical energy, the only possible trajectories that remained are those traveling away from the fixed point (i.e. the unstable manifold). The chaotic behavior is due to striking these points directly and can be seen by noting the singularities in Figure 5.1(top) around $b = \pm 1$.

With this geometry in mind we are ready to discuss the linear behavior of the system above the critical energy. We start with the definition of the Lyapunov exponent in terms of separation of nearby trajectories:

$$d_t = d_0 e^{\lambda t} \qquad [6.2\text{-}1]$$

where d_t is the separation at some time (t), d_0 is the initial separation of the two trajectories, and λ is the Lyapunov exponent. Next we write the Lyapunov exponent in terms of the energy. Since we are above the critical energy, we can use the linear form:

$$\lambda = b + mE \qquad [6.2\text{-}2]$$

where b is the intercept and m is the slope. Combining these two equations results in the separation as a function of time and energy:

$$d_t(E,t) = d_0 e^{(b+mE)t} \qquad [6.2\text{-}3]$$

we have added the explicit functional dependence of the separation for clarity. We now look at two different energies, E_1 and E_2, with E_2 being the larger of the two. Two nearby trajectories (of the same energy) diverge in time at two different energies as:

$$d_t(E_1,t) = d_0 e^{(b+mE_1)t} \qquad [6.2\text{-}4]$$

$$d_t(E_2,t) = d_0 e^{(b+mE_2)t} \qquad [6.2\text{-}5]$$

we now compare the separation as a function of time for these two energies (dividing Equation 6.2-5 by 6.2-4):

$$\frac{d_t(E_2,t)}{d_t(E_1,t)} = \frac{d_0 e^{(b+mE_2)t}}{d_0 e^{(b+mE_1)t}} = e^{m(E_2-E_1)t} \qquad [6.2\text{-}6]$$

We solve the above equation for the separation in time of with starting energy E_2:

$$d_t(E_2,t) = d_t(E_1,t)\, e^{m(E_2-E_1)t} \qquad [6.2\text{-}7]$$

While this looks very similar to Equation 6.2-1, there is one big difference: $d_t(E_1,t)$ changes over time and is not constant. We consider this to be a local effect.

Note that the right hand side of this equation is greater than $d_t(E_1,t)$ because E_2-E_1 is greater than zero, the slope is always positive, and time is positive, so the exponential will be greater than unity. We also know that this must be the case

because E_2 will have a larger Lyapunov exponent than E_1. Equation 6.2-7 indicates that the rate of divergence of the higher energy trajectory will grow exponentially faster than the lower energy one

The slope (along with the energy separation), gives a measure of how much faster the higher energy trajectories diverge when compared to the lower energy ones. The slope measures the rate of divergence between rates of separation at different energies.

Because this higher energy chaos is from a direct collision, it is the exact shape of energy space that will determine the slope of the linear response. We know from looking at the results of these fits, that most of these potentials do not have the same slope. We conclude that most of these potential systems do not have the same energy space shape at high energy. The most notable exception to this is the three with an all positive front face: V_1, V_{2A}, and V_{5B}. Also V_{2C} and V_{4A} have almost identical slopes. Those that have similar slopes will have similar high energy chaotic sets.

6.3. FUTURE WORK

6.3.1. New potentials

For each of our potentials, we kept the incident beam parallel to the x-axis. However, to complete the investigation of this type of system, we need to examine other incident angles. In particular, those along y=x and y=-x would be of importance. In the figure below we begin with the six unrotated potentials and indicate all of the symmetry axis that could be investigated. The paths that represent

the previously studied ten potentials have been given the name used in this experiment.

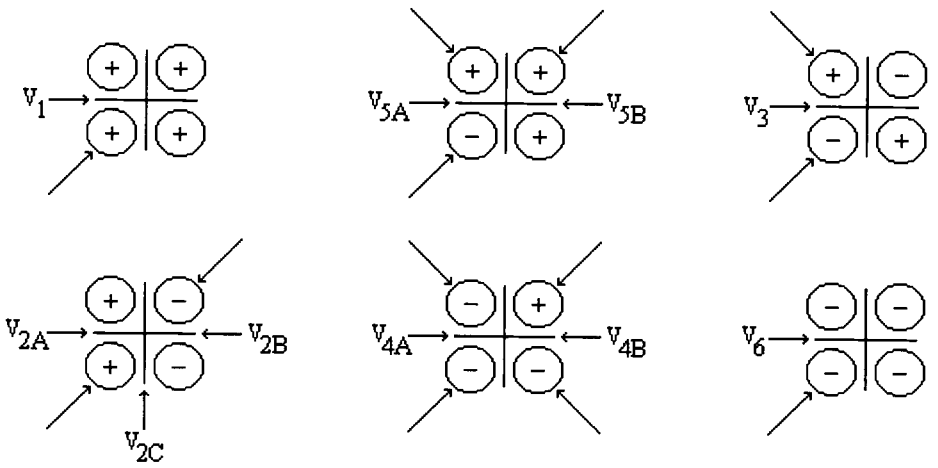

Figure 6.1 - Possible impact axes along symmetry lines for the various four hill potentials. Those that have already been studied in this experiment are given the familiar label. The ones that are unlabeled are possibilities for future study.

This would result in thirteen new potentials to investigate. In our original project, we did some preliminary work using V_3 in such an off axis configuration. We found that if the positive hill was sticking out in front, the scattering functions had almost no singularities. In contrast, if the negative hill was out in front, the system was very chaotic. It would be of interesting if the other potentials had this behavior as well.

6.3.2. Code improvements

Most of the improvements to our experiment would be in the software programs themselves. The sheer size of this experiment made for long computation times. The majority of these runs were performed on the Beowulf cluster, at Oregon State University. The basic experiment of finding the scattering angle (or delay time) as a function of impact parameter was relatively fast (approximately three hours for each potential). It took about 48 hours to calculate the Lyapunov exponents for a single potential. The capacity dimension experiments took over 200 hours for each potential. In the end it took over 104 computational days (2500 hours) of production quality runs to generate the data used in this paper. We were very fortunate that the Beowulf (20 machines) and the Berrypatch (17 machines) were both available. Any small improvements in efficiency would have large effects on these times.

We would start by converting the code into C++ executables. These natively compiled programs would run mach faster than the JVM (Java Virtual Machine) interpreter. This process would not be terribly difficult because of how similar the language for Java and C++ actually are. We would use C++ over C because of the object-oriented nature of our original code.

We now turn our attention to the methods for calculating the Lyapunov exponent. The most commonly used methods for calculating the exponent involve finding trajectories that are arbitrarily close to the stable manifold. The fastest of these methods is called the Stagger-and-Step (33). Since we have found that our brute force method yields comparable results to the published results, we would be justified in using this more elegant method.

Finally, any improvement in the convergence of the capacity dimension calculations would have a huge impact on the total computational time. The uncertainty exponent technique, as discussed in Section 4.3, is very effective for

capacity dimensions close to unity. But it takes approximately ε^{-1} trajectory pairs (from Equation 4.3-4) when the capacity dimension is almost zero. A technique has been developed, called OFE (36), which converges as ε^{-d}. This method would be much better for low values of the capacity dimension.

6.3.3. Further high energy study

We are interested to see if the high energy, linear, behavior of the Lyapunov exponent is a general characteristic of any other type of chaotic scattering. This linear trend has not been reported before. The standard methods used to calculate the exponent, simply would not work if there is no possibility of a trapped orbit. We believe that this linear behavior would be observed in other abrupt bifurcation systems at the very least.

REFERENCES

1. R. Hilborn, *Chaos and Nonlinear Dynamics*, Oxford University Press, Oxford, 1994.

2. E. Ott, Chaotic scattering: an introduction, Chaos 3 (1993) 417.

3. V. Daniels, M. Vallières, and J. M. Yuan, Chaotic scattering on a double well: periodic orbits, symbolic dynamics, and scaling, Chaos 3 (1993) 475.

4. J. M. Yuan and Y. Gu, Chaotic electronic scattering with He^+, Chaos 3 (1993) 569.

5. B. Eckhardt and C. Jung, Regular and irregular potential scattering, J. Phys. A 19 (1986) L829.

6. L. Gottdiener, The multiple-collision region in non-attractive atom-diatom collisions, Mol. Phys. 29 (1999) 1585.

7. E. Ziemniak, C. Jung, T. Tél, Physica D 76 123 (1994) 2191.

8. B. Eckhardt and H. Aref, Integrable and chaotic motions of four vortices II, Phil. Trans. R. Soc. London 326 (1988) 655.

9. S. Bleher, C. Grebogi, E. Ott, Bifurcation to chaotic scattering, Physica D 46 (1990) 87.

10. Y.-C. Lai, Abrupt bifurcation to chaotic scattering with discontinuous changes in fractal dimension, Phys. Rev. E (60) 6 (1999) R6283.

11. R. Scheck, *Mechanics: from newton's laws to deterministic chaos*, Springer-Verlag, New York, 1994..

12. S. Bleher, C. Grebogi, E, Ott, and R. Brown, Fractal boundaries for exit in Hamiltonian dynamics, Phys. Rev. A (38) 2 (1988) 38.

13. D. Sweet and E. Ott, Fractal dimension of higher-dimensional chaotic repellors, Physica D 139 (2000) 1.

14. Q. Chen, M. Ding, and E. Ott, Chaotic scattering in several dimensions, Phys. Lett. A. 145 (1990) 93.

15. C. Jong and H-J Scholz, Scattering off a magnetic dipole, J. Phys A: Math. Gen. 21 (1998) 2301.

16. Y.-C. Lai, A. de Moura, and C. Grebogi, Topology of high-dimension chaotic scattering, Phys. Rev. E. (62) 5 (2000) 6421.

17. M. Ding, C. Grebogi, E. Ott, and J.A. Yorke, Transition to chaotic scattering, Phys. Rev. A 42 (1990) 7025

18. C. Grebogi, E. Ott, and J. Yorke, Super persistent chaotic transients, Ergodic Theory and Dyn. Sys. 5 (1985) 341.

19. M. Ding, C. Grebogi, E. Ott, and J. Yorke, Massive bifurcation of chaotic scattering, Phys. Lett. A 153 (1991) 21.

20. Q. Chen, and E. Ott, Chaos in several dimensions, Phys. Lett. A, 144 (1991) 93.

21. R. Haberman and D. Diminnie, Slow passage through a saddle-center bifurcation, J. Nonlin. Sci.10 (2000) pp. 197.

22. K. Życzkowski and Y.-C. Lai, Devil-staircase behavior of dynamical invariants in chaotic scattering, Physica D 142 (2000) 197.

23. M. Ding, C. Grebogi, E. Ott, and J. A. Yorke, Massive bifurcation of chaotic scattering, Phys. Lett. 153A (1991), 21-26.

24. J.. Eckmann and S. Kamphorst, Liapunov exponents from time series, Phys. Rev. A 34 (1986) 4971.

25. A. Wolf, J. Swift, H. Swinney, and J. Vastano, Determining Lyapunov exponents from a time series, Phys. 16D (1985) 285.

26. Classical Dynamics of Particles and Systems 4th ed., Marion and Thorton, Saunders College Publishing, New York, 1995, p183.

27. M. Tabor, *Chaos and Integrability in Nonlinear Dynamics: An Introduction*, Wiley Interscience, New York, 1987.

28. H. Kandrup, C. Siopis, G. Contopoulos, and R Dvorak, Diffusion and scaling in escapes from two-degrees-of-freedom Hamiltonian systems.

29. H. Kandrup, Geometric interpretation of chaos in two-dimensional Hamiltonian systems, Phys. Rev. E. (32) 9 (1997) 2272. E.

30. P. Grassberger, R. Badii, and A. Politi, Scaling laws for invariant measures on hyperbolic and nonhyperbolic attractors, J. Stat. Phys. 51, 135 (1988).

31. H. Nusse and J. Yorke, Analysis of a procedure for finding numerical trajectories close to chaotic saddle hyperbolic sets, Ergod. Th. & Dynam. Sys. 11 (1991) 189.

32. D. Sweet, H. Nusse, and J. Yorke, Stagger-and-step method: detecting and computing chaotic saddles in higher dimensions, Phs. Rev. Lett. 11 (2001) 2261.

33. A. Wolf, J. Swift, H. Swinney, and J. Vastano, determining lyapunov exponents from a time series, Phys. 16D (1985) 285.

34. J.M. Green and J-S. Kim, Lyapunov exponent of a many bodied system, Physica D 24 (1987) 213.

35. M. Rosenstein, J. Collins, and C. De Luca. A practical method for calculating largest Lyapunov exponents from small data sets, Physica D 65 (1993) 117.

36. A. de Moura and C. Grebogi, Output functions and fractal dimensions in dynamical systems, Phys. Rev. Lett. (86) 13 (2001) 2778.